

Optical and NIR spectroscopy of cool CEMP stars to probe the nucleosynthesis in low mass AGB binary system

A. Susmitha¹*, D.K. Ojha¹, T. Sivarani², J.P. Ninan³, A. Bandyopadhyay⁴,

Arun Surya⁵, Athira Unni²

¹Tata Institute of Fundamental Research, Colaba, Mumbai- 400005, India

²Indian Institute of Astrophysics, Koramangala II block-560034, Bengaluru, India

³Dept. Of Astronomy and Astrophysics, 525 Davey Lab, Pennsylvania State University, University Park, 16802, The United States.

⁴Aryabhata Research Institute of Observational Sciences, Manora Peak, Nainital-263001, India

⁵Center for Astrophysics And Space Sciences, University of California, San Diego, 92093, The United States

Accepted XXX. Received YYY; in original form ZZZ

ABSTRACT

We present the abundance analyses of 7 Carbon enhanced metal-poor (CEMP) stars to understand the origin of carbon in them. We used high-resolution optical spectra to derive abundances of various elements. We also used low-resolution Near-Infrared (NIR) spectra to derive the abundance of O and ¹²C/¹³C from the CO molecular band and compared their values with those derived from high-resolution optical spectra. We identified a good agreement between the values. Thus, in cool CEMP stars, the NIR observations complement the high-resolution optical observations to derive the oxygen abundance and the ¹²C/¹³C ratio. This enables us to probe fainter cool CEMP stars using NIR spectroscopy. C, N, O abundances of all the program stars in this study show abundances that are consistent with binary mass transfer from a low-mass low-metallicity Asymptotic Giant Branch (AGB) companion which is further supported by the presence of enhancement in neutron-capture elements and detection of radial velocity variation. One of the stars show abundance patterns similar to a CEMP-*s* star whereas the abundance pattern of the rest of the stars satisfy the criteria required to classify them as CEMP-*r/s* stars. The sub-classification of some of the stars studied here is revisited. The abundance of neutron-capture elements in these CEMP-*r/s* stars resembles to that of *i*-process models where proton ingestion episodes in the companion low-mass low-metallicity AGB stars produce the necessary neutron density required for the onset of *i*-process.

Key words: CEMP-*r/s*- AGB companion – *i*-process– NIR spectroscopy

1 INTRODUCTION

Spectroscopic studies of metal-poor stars identified from early large surveys like Hamburg/ESO survey and HK survey brought out the fact that a significant fraction of Galactic halo stars exhibit strong enhancement in carbon with [C/Fe] >+0.7¹ (Beers et al. 1992; Christlieb et al. 2001; Aoki et al. 2007; Yanny et al. 2009). The fraction of so called carbon enhanced metal-poor [CEMP] stars increases with decreasing metallicity (Lucatello et al. 2005, 2006; Aoki et al. 2007, 2013; Yong et al. 2013; Placco et al. 2014) and

it is of great interest due to their high carbon abundance and the sizable fraction in the low-metallicity regime. Various follow-up studies have revealed that these CEMP stars also show peculiar elemental abundance pattern along with the strong over abundance in C. Based on these peculiar abundance pattern, CEMP stars are broadly classified into two categories (Beers & Christlieb 2005; Jonsell et al. 2006; Aoki et al. 2007; Masseron et al. 2010); one shows over abundance of neutron capture elements including the elements from slow neutron-capture process (*s*-process) or/and rapid neutron-capture (*r*-process) process (CEMP-*s*, CEMP-*r*, CEMP-*r/s*) and other does not show any enhancement in neutron capture elements (CEMP-*no*).

Among the CEMP population, CEMP-*s* sub-class constitutes around 80% of the population in the metal-rich end (Aoki et al. 2007; Hansen et al. 2016b, based on their sample of ~40 stars altogether) and multi-epoch observations of these stars reported that majority of stars in the CEMP-*s* class are members of binary systems (Lu-

* E-mail: susmitha.antony@tifr.res.in (AS)

¹ The abundance of one element with respect to another is expressed by the comparison of their ratios with respect to the sun and is indicated as, [A/B] = log₁₀(N_A/N_B)* – log₁₀(N_A/N_B)_⊙, where N_A and N_B are the number densities of elements A and B and * and ⊙ denote the stellar and solar values.

catello et al. 2005; Starkenburg et al. 2014). This favors the idea of mass transfer from a companion AGB star which is more massive compared to the primary and therefore would have evolved to a cool white dwarf (Bisterzo et al. 2012; Abate et al. 2015, and references therein). For the case of CEMP-*r* stars, only a few of them are known till date (Snedden et al. 2003; Hansen et al. 2015) and the possible origin of *r*-process elements in this subclass include supernovae (SNe) nucleosynthesis (Wheeler et al. 1998; Qian & Wasserburg 2007; Sneden et al. 2008; Winteler et al. 2012) and/or neutron star merger events (Lattimer & Schramm 1974; Thielemann et al. 2017; Watson et al. 2019). There are also CEMP-*r/s* stars, that constitute relatively a larger fraction compared to CEMP-*r* stars, exhibiting enhancement in *r*- and *s*-process elements. They also show radial velocity variations, hence two different sources for such enrichment of *s*- and *r*-process elements are considered. Some hypothesize that carbon and *s*-process abundance would have similar origin as that of the CEMP-*s* stars (Sivarani et al. 2004; Masseron et al. 2010; Bisterzo et al. 2011) whereas the origin of *r*-process elements is considered to be from SNe or neutron-star mergers which pre-enrich the birth cloud of the binary stars with *r*-process elements (Bisterzo et al. 2012). This two-source pollution could not satisfactorily explain the observed number of CEMP-*r/s* stars as well as the correlation between the enrichment in the *s*-process and *r*-process elements (Abate et al. 2015). Recently, nuclear network calculations using neutron densities halfway between *s*- and *r*-processes were able to produce the abundance pattern similar to CEMP-*r/s* stars (Hampel et al. 2016; Denissenkov et al. 2017) thus invoking the possibility of a single stellar site for the production of *s*- and *r*-process in CEMP-*r/s* stars instead of two-source pollution. In the literature sometimes CEMP-*r/s* stars are referred as CEMP-*i* stars because the intermediate neutron-capture process seems capable of reproducing the mixed *s*- and *r*- process abundance pattern. While majority of the CEMP population exhibit the signatures of a binary companion, CEMP-*no* stars are often found not to be associated with binaries (Hansen et al. 2016a) thus they reflect the ISM abundance from which the star was born. Also, CEMP-*no* stars are found to be dominating the CEMP population at lower metallicities (Salvadori et al. 2015). Models of faint SNe that experienced mixing and fallback and models of zero-metallicity-spin stars having high rotational velocity are some of the proposed scenarios for explaining the peculiar abundance patterns shown by CEMP-*no* stars (Umeda & Nomoto 2003; Meynet et al. 2006; Yoon et al. 2016; Hansen et al. 2016a). These progenitors expel huge amount of C,N and O to the ISM.

Despite various astrophysical processes are identified as a source for carbon in CEMP-*r/s* stars, the masses of progenitors and multiple nucleosynthetic processes or their sites to explain the diverse abundance pattern of the light and heavy elements are still unclear. To fully understand the sites and mechanisms that contribute the enrichment of light and heavy elements in CEMP-*r/s* we require measurements of C, N and O for a large sample of CEMP stars along with other elemental abundances. The abundance of C and N can be determined from low-resolution optical spectra of CEMP stars using the CH, C₂ and CN features. But O abundance measurements require high-resolution spectroscopy. Typical high-resolution oxygen abundances are made from the forbidden [OI] lines at $\lambda 6300$, $\lambda 6363$ and O I triplet near $\lambda 7774$. However, the O I triplet lines at $\lambda 7774$ are strongly affected by non-local thermodynamic equilibrium (NLTE) and local thermodynamic equilibrium (LTE) approximation results in over estimation of the abundances (Asplund et al. 2005; Amarsi et al. 2016, 2019). But the forbidden [OI] lines at $\lambda 6300$ and $\lambda 6363$ do not show any significant departures from LTE

even though they do suffer from 3D effects. These 3D effects cause an abundance variation maximum up to 0.2 dex (Caffau et al. 2015; Amarsi et al. 2016). Hence, more reliable abundance measurements thus come from the forbidden [O I] lines at 6300\AA and 6363\AA . But these lines are very weak at lower metallicities and it requires hours of exposures to detect the feature (Schuler et al. 2006). Many cool CEMP stars are unexplored due to the complexity of analysis and need for high resolution high S/N data. But the near-infrared (NIR) first-overtone ro-vibrational bands of CO at $2.3\ \mu\text{m}$ gives a possible alternate to this problem because of their detection even at lower resolution (Beers et al. 2007; Kennedy et al. 2011; Hansen et al. 2019a). In CEMP stars, the C/O ratio is > 1.0 i.e; the carbon abundance exceeds the oxygen abundance. So essentially all the oxygen would be locked up in CO molecules and these NIR lines will provide a sensitive probe for the oxygen abundance in CEMP stars.

The carbon isotopic ratio $^{12}\text{C}/^{13}\text{C}$ is an important parameter to understand the degree of mixing in the progenitors or the observed star itself (Spite et al. 2005, 2006; Sivarani et al. 2006) and is usually derived from the optical spectra using the $^{12}\text{C}_2$ band head at $4737\ \text{\AA}$ and the $^{12}\text{C}^{13}\text{C}$ band head at $4744\ \text{\AA}$. But in cool stars, the $^{12}\text{C}_2$ band head at $4737\ \text{\AA}$ may be saturated and leads to a large derived $^{12}\text{C}/^{13}\text{C}$ ratio. This problem can be resolved by using the CO features at $2.3\ \mu\text{m}$ where the ^{13}CO lines are well separated from the ^{12}CO lines. So it provides an accurate and better estimates of the mixing diagnostic $^{12}\text{C}/^{13}\text{C}$ ratio than deriving it from the optical spectra (Beers et al. 2007), for cool CEMP stars.

In this paper, observations of 7 CEMP stars are reported to understand the origin of various elements in them and to validate the oxygen abundances derived from NIR spectra with that of [OI] $\lambda 6300$ line in optical. The paper is organized as follows: In section 2, sample selection and observation have been mentioned. Section 3 and section 4 describe the details of stellar parameters and abundance analysis. In section 5, the results are discussed with how the companion's properties can be constrained with the abundance pattern of light and heavy elements and in section 6, the paper is concluded.

2 OBSERVATION AND DATA REDUCTION

One of the motivations of this study is to measure the C, N and O abundances, and compare the oxygen abundance from CO features in the NIR regime and oxygen from [OI] at $6300\ \text{\AA}$. So the target selection considered were, metal poor stars that are enhanced in carbon abundance, low effective temperature ($T_{\text{eff}} < 5000\text{K}$) and $V_{\text{mag}} < 13$, suitable for observations using a 2m class telescope. At such cool temperatures and with $\text{C/O} > 1$, all the oxygen will be locked up as CO molecule. So the program stars were chosen from literature where the carbon has been previously measured which has low effective temperature. The details of the targets are given in the table 1.

The targets were observed using the TIFR (Tata Institute of Fundamental Research) Near Infrared Spectrometer and Imager (TIRSPEC) (Ninan et al. 2014) and Hanle Echelle Spectrograph (HESP) (Sriram et al. 2018) mounted on 2m Himalayan Chandra Telescope (HCT), Hanle. TIRSPEC was used to capture the CO bands at $2.3\ \mu\text{m}$ and HESP was used for the optical observations. The NIR spectra have been taken in the cross-dispersed mode using a slit S3 (width is $1.97''$). This setup covers both the H and K bands simultaneously, covering a wavelength of $1.50 - 1.84\ \mu\text{m}$ & $1.95 - 2.45\ \mu\text{m}$ at a resolution $R \sim 800$. Dithering along the slit was performed for accurate background subtraction, we also avoided regions of bad pixels by suitably choosing the target location on the slit. A0

Table 1. The details of the program stars.

Star	RA (J2000)	DEC (J2000)	Vmag	Kmag	MJD	RV_{helio} (kms^{-1})	SNR at $2.1 \mu\text{m}$	SNR at 4800 \AA	Reference:
HD 5223	00:54:13.61	+24:04:01.52	8.5	5.7	57775.68434693	-242.9	66.3	58.2	1
HE 0314-0143	03:17:22.18	-01:32:36.51	12.6	8.0	57784.59031674	-33.6	45.3	27.5	1,2
HE 1152-0355	11:55:06.06	-04:12:24.71	11.4	8.4	57801.81004023	428.6	36.2	26.7	1,2
HE 0017+0055	00:20:21.60	+01:12:06.83	11.7	8.5	58720.81863073	-83.2	33.8	56.1	1,2
BD+42 2173	11:00:00.44	+41:36:07.50	8.1	7.4	58575.57389648	-59.9	61.6	50.2	1
HD 187216	19:24: 18.35	+85:21:57.19	9.6	6.0	58575.85302417	-122.4	44.7	51.6	1
HE 1418+0150	14:21:01.15	+01:37:17.76	12.2	9.1	57801.97132139	-22.4	44.6	26.2	1,2

References: 1: [Masseron et al. \(2010\)](#); 2: [Kennedy et al. \(2011\)](#) and references therein.

type stars at the same air mass were also observed along with the targets to correct for the telluric lines in the spectra. In order to avoid the counts reaching the non-linearity regime of the detector, the observations were performed as multiple exposures of 500sec. The final spectrum thus obtained had a signal to noise ratio (SNR) ~ 30 . The NIR data reduction has been performed using semi automated pipeline developed by [Ninan et al. \(2014\)](#) in which the dark correction, flat fielding, background subtraction, spectrum extraction, wavelength calibration, telluric line correction and continuum fitting were performed using codes in python which made use of standard modules like astropy, numpy, matplotlib and PyRAF².

The optical observations of the program stars were taken in high-resolution ($R = 30000$) using HESP. They were observed in multiple frames of 45 minute exposures depending on the brightness and obtained the spectra in the star-sky mode which enabled the sky to be subtracted from the object fibre. ThAr spectrum was taken along with each program star spectrum for the wavelength calibration. The spectral reduction included, trimming, bias subtraction, aperture extraction and wavelength calibration. These steps were performed using PyRAF. The final normalized and co-added spectrum covers a wavelength range from 4000-10500 \AA .

3 STELLAR PARAMETERS AND CHEMICAL ABUNDANCES

The spectra of all the program stars are dominated by molecular features because of high carbon abundance and low effective temperature. This hindered us from getting clean lines of iron (Fe) for estimating the stellar parameters using equivalent width method. So, we performed a full spectrum synthesis to derive abundances from the atomic lines.

We used the spectral synthesis code TURBOSPECTRUM developed by [Plez \(2012\)](#) to derive abundances and obtain the stellar parameters. We used the stellar atmospheric models by [Mészáros et al. \(2012\)](#) in which the ATLAS9 and MARCS codes were modified with an updated H_2O linelist and with a wide range of carbon- and α -element enhancements. Whenever required, we interpolated the models from the grid of model photospheres provided by [Mészáros et al. \(2012\)](#) to obtain the intermediate parameter values. LTE has been assumed for all species. But we referred [Mashonkina et al. \(1999\)](#); [Mashonkina & Gehren \(2000\)](#); [Andrievsky et al. \(2009, 2010\)](#); [Lind et al. \(2011\)](#); [Mashonkina & Christlieb \(2014\)](#) and [Hansen et al. \(2020\)](#) for NLTE corrections of various elements

and whenever available we applied their corrections to the derived abundances. We adopted the Solar abundances from [Asplund et al. \(2009\)](#) and Solar isotopic ratios were used unless otherwise specified. The line lists for atomic lines were assembled from the Vienna Atomic Line Database (VALD) database ([Kupka et al. 1999](#)) and the details of the same are mentioned in the table A1. Hyperfine structure (HFS) has been accounted for Li, Sc, Ba, La and Eu. For the case of molecular linelists, we used the CH line list compiled by T. Masseron (priv. comm.) and CN data from [Plez & Cohen \(2005\)](#). The linelists for C_2 and NIR CO molecular features were taken from the Kurucz database³.

3.1 Stellar parameters

The effective temperatures of all the program stars were calculated from J-H, J-K and V-K colors using various color transformation relations ([Alonso et al. 1996, 1999](#); [Ramírez & Meléndez 2005](#)). For this, whenever available, we used the metallicity quoted in the literature as the initial metallicity of the respective star and the reddening values, $E(B-V)$, from [Schlegel et al. \(1998\)](#). The derived photometric temperature values are consistent within 150K. Among these, the temperature derived from the V-K color index is considered superior due to its large span in the wavelength of the bands involved. Also, these bands are relatively free from contamination from molecular C. So we adopted the temperature derived from the V-K color as the star's temperature which is also consistent within 150K with literature values. Hence, we adopt this value as uncertainty in the temperature measurements, for deriving abundances. We have also cross-verified the temperature of the star using the available data from *Gaia* data release 2⁴. The available *Gaia* temperatures are matching within the error (± 150 K).

The surface gravity, $\log g$, was derived by fitting the wings of Mg I triplet around 5172 \AA using a synthetic grid of model spectra where we adopted the temperature derived from the above method as the model temperature value and for various values of $\log g$ with a step size of 0.25 dex. The best fit value was found by the goodness of the fit and chosen as the final $\log g$. While fixing $\log g$, we also changed the carbon abundance from $[\text{C}/\text{Fe}] = 0.0$ to $[\text{C}/\text{Fe}] = +1.5$ to simultaneously fit the C_2 band-head at 5165 \AA to converge on to the best fit parameters. We have checked the effect of carbon abundance on the wings of Mg I lines by fitting the Mg I lines with different values of $[\text{C}/\text{Fe}]$. The effect is found to be negligible (refer figure B1). We identified that the $\log g$ of the program stars ranges from 0.25 to 1.9. In order to understand the evolutionary phase of the program

² PyRAF is a product of the Space Telescope Science Institute, which is operated by AURA for NASA

³ <http://kurucz.harvard.edu/linelists/linesmol/>

⁴ <https://gea.esac.esa.int/archive/>

Table 2. The atmospheric parameters of the program stars from this study. The uncertainties in the measurements of stellar parameters is also mentioned in the table.

star name	T_{eff} K ± 150	$\log g$ cms^{-2} ± 0.25	[Fe/H] dex ± 0.2	ξ kms^{-1} ± 0.2	type
HD 5223	4335	1.20	-2.1	2.0	r/s
HE 0314-0143	3881	0.25	-1.9	2.1	r/s
HE 1152-0355	4200	0.25	-1.7	2.2	s
HE 0017+0055	4240	1.00	-2.6	1.9	r/s
HE 1418+0150	4150	1.80	-2.0	2.0	r/s
BD+42 2173	4430	1.90	-1.6	1.5	r/s
HD 187216	3920	0.80	-2.5	2.0	r/s

stars, we obtained the luminosity of the stars from *Gaia* DR2 data and placed the stars on their respective isochrones from BASTI stellar evolution database (Pietrinferni et al. 2004) and identified that all the program stars fall in the upper part of the red giant branch (RGB). The metallicities of the stars were derived by fitting the iron features in the visual spectra where the molecular features have less influence on the continuum (e.g., Fe lines in the range 5190 Å - 6450 Å). The best fit value was chosen as the final value with an error of ± 0.2 dex. The uncertainty was chosen in such a way that the best fit does not change while changing the Fe abundance. We derived the microturbulence velocity (ξ) by simultaneously matching the iron abundance of weak and strong FeI lines in the spectra. We fitted the unblended iron features by varying the ξ by a step-size of 0.2 kms^{-1} and the best fit value was taken as the final microturbulent velocity. The final adopted stellar parameters with the uncertainty in measurements are listed in the table 2

4 ABUNDANCES

The abundances of key elements such as Li, C, N, O, Mg, Na, Ca, Y, Ba, Eu and Sm were derived using the spectral synthesis method where the input model parameters were chosen from the table 2. Using these model parameters, the synthetic spectral grid was generated by varying the input elemental abundances in steps of 0.2 dex. This synthetic spectra were used to fit the respective spectral line and the best fit value was chosen as the final abundance. The derived abundances are quoted in the table 3. The details of the abundance measurements for each element are briefly described below.

4.1 Uncertainties in the abundance measurements

The stellar parameters and the elemental abundances are estimated using spectral synthesis method. So, the uncertainty in the abundance values was estimated through the goodness of the least squares fit and are mentioned in the table 4.

The systematic errors in our abundances were derived using models where each stellar parameter (T_{eff} , $\log g$, ξ) was varied by a fixed amount (± 150 K, ± 0.25 dex, ± 0.2 km s^{-1}) while keeping other parameters constant and from those, new abundances were computed. To perform the analysis, we choose HD 5223 as the representative star for the program stars in this study. The resulting change on abundance variations upon these parameter variations as well as their combined effect, calculated by adding them in quadrature, are listed in the table 4.

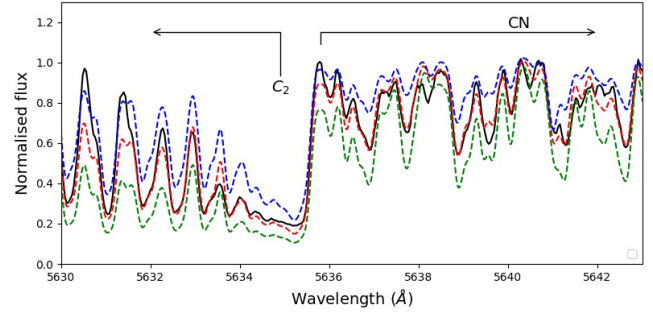


Figure 1. The region of C₂ band head at 5635 Å and the CN molecular features of HD 187216 are fitted with the synthetic spectra. The arrows indicate the region where the respective features are present. The spectrum shown in black is the observed data, whereas the spectrum in red corresponds to the best fit value [C/Fe] = 1.45 and [N/Fe] = 0.93. Green and blue lines indicate syntheses corresponding to the range of uncertainty of ± 0.2 dex in both carbon and nitrogen abundances.

4.2 C, N and O

The carbon abundance in the program stars has been derived by fitting the C₂ molecular band heads at 5165 Å and 5635 Å. Both features yielded the same abundance values and we adopted this carbon value while deriving the abundances of N and O from molecular features. For the case of N abundance, we used CN lines in the wavelength range from 5635-6700 Å by iteratively changing the nitrogen abundance of the synthetic spectra by 0.2 dex and fixed the carbon abundance to the value derived from C₂ molecular band and fitting the entire spectral region (refer figure 1). The best-fit value is chosen as the final nitrogen abundance. We did not use strong CN lines in the blue region at 4215 Å due to the poor the SNR.

The oxygen abundance from optical spectra was derived by using the [O I] lines at 6300, 6363 Å. Since these lines are blended with CN features, a small change in the nitrogen abundance affects the derived oxygen abundance. So, the carbon abundance and the nitrogen abundance were first fixed to be the value obtained from the C₂ and CN bands and the oxygen abundance was iteratively adjusted to fit the [O I] lines. While fixing the O abundance, N abundance was also iteratively changed by a small amount for a better fitting of the [OI] feature but without affecting the nearby CN features. The resulting O abundance from both the lines differs by 0.3 dex because of the iterative process involving both N and O, and we take this difference as our final uncertainty on the reported oxygen abundances. The spectral fitting of the [OI] line is shown in the figure 2. The oxygen abundance from NIR CO molecular features at 2.3 μm were also obtained for all the program stars in this study. The C and N abundance derived from optical spectra were kept fixed in the synthetic spectral grid and we varied the oxygen abundances with a step size of 0.2 dex and the best fit value was chosen as the final value (see figure 3). The final C, N and O abundances were listed in the table 3 and the oxygen abundances derived from both optical and NIR spectra are compared in the figure 4. The O abundance from optical and NIR are matching within an uncertainty of 0.3 dex. So the average of these two values was used as O abundance elsewhere in the text.

Table 3. The $[X/Fe]$ of various elements are reported in the table. The corresponding 1σ uncertainty in the abundance measurements, $\sigma_{\log\epsilon(X)}$, is mentioned in the last column.

Element	Solar	HD 5223	HE 1152-0355	HE 1418+0150	BD+42 2173	HD 187216	HE 0017+0055	HE 0314-0143	$\sigma_{\log\epsilon(X)}$
Li [§]	1.05	<0.00	<0.00	<-0.05	<0.00	<0.00	<-0.10	<-0.50	0.30
C	8.43	1.35	1.35	1.30	1.10	1.45	2.10	0.95	0.20
N	7.83	0.73	0.95	1.20	1.00	0.93	1.65	0.55	0.20
O	8.69	0.35	0.50	1.00	0.35	0.05	0.90	1.02	0.30
Na (LTE)	6.24	0.20	-0.10	0.60	0.80	0.50	0.70	0.30	0.20
Na (NLTE)	6.24	0.13*	—	0.45*	0.60*	—	0.61*	0.20*	0.20
Al	6.45	< -0.00	<-0.20	<-0.40	0.65	<-0.10	<0.00	<-0.00	0.30
Mg	7.60	-0.10	0.40	0.10	0.40	0.30	0.00	0.40	0.20
K(LTE)	5.03	...	0.70	0.10	0.80	0.10	0.60	0.00	0.20
K (NLTE)	5.11	...	—	-0.26 *	0.27 *	0.09*	0.40*	—	0.20
Ca	6.34	0.10	0.30	-0.20	0.40	0.30	0.30	0.00	0.30
Sc	3.15	0.25	0.00	0.70	0.40	0.90	0.85	0.35	0.20
Rb	2.52	0.60	<-0.30	<-0.50	0.70	< 0.10	<0.10	0.60	0.20
Y	2.21	0.80	0.40	1.10	1.40	0.80	0.50	0.55	0.20
Zr	2.58	1.30	0.40	1.50	1.20	1.50	1.70	0.80	0.20
Ba	2.18	1.50	1.30	1.80	2.20	2.00	2.30	1.35	0.20
La	1.10	1.70	1.40	2.00	2.20	2.00	2.30	1.65	0.20
Ce	1.58	1.42	1.20	2.10	2.00	1.90	2.00	1.07	0.20
Pr	0.72	1.48	1.18	2.30	2.10	1.98	2.20	1.25	0.20
Nd	1.42	1.48	1.20	1.90	2.10	1.66	2.20	1.35	0.20
Sm	0.96	1.24	0.90	1.50	2.00	1.64	2.10	1.09	0.20
Eu	0.52	1.06	<0.36	1.16	1.60	1.66	1.96	1.23	0.20
$[hs/ls]$	0.00	0.49	0.90	0.70	0.83	0.85	1.10	0.68	—

The * represents the values corrected for the NLTE effects and — represents no available NLTE correction.

§ The Li abundance quoted here is in the absolute scale, $A(\text{Li})$

Table 4. The variation of abundances upon the variation of stellar parameters are mentioned here. The last column is the resulting change in the abundances due to the combined effect which is obtained by adding individual variations in quadrature.

Element	$\Delta\log\epsilon(X)$			$\sigma_{\text{sys}}^{\text{tot}}$
	ΔT_{eff} ($\pm 150\text{K}$)	$\Delta\log g$ (± 0.25 dex)	$\Delta\xi$ ($\pm 0.2\text{km s}^{-1}$)	
Li	± 0.3	∓ 0.15	± 0.0	0.11
O	∓ 0.1	∓ 0.05	± 0.0	0.01
Na	∓ 0.05	± 0.10	∓ 0.05	0.02
Al	∓ 0.15	± 0.10	∓ 0.05	0.04
Mg	± 0.0	± 0.1	± 0.0	0.01
K	± 0.1	± 0.05	± 0.0	0.01
Ca	± 0.1	∓ 0.1	± 0.0	0.02
Sc	± 0.0	∓ 0.05	∓ 0.05	0.01
Rb	± 0.1	± 0.0	± 0.05	0.01
Y	± 0.05	± 0.05	± 0.0	0.01
Zr	± 0.1	± 0.0	± 0.0	0.01
Ba	± 0.15	± 0.1	± 0.0	0.03
La	± 0.0	∓ 0.05	± 0.0	0.01
Ce	± 0.05	± 0.05	± 0.0	0.01
Pr	± 0.15	± 0.05	± 0.05	0.03
Nd	± 0.05	± 0.05	± 0.0	0.01
Sm	± 0.1	± 0.1	± 0.0	0.02
Eu	± 0.2	± 0.1	± 0.0	0.05

4.3 Li and $^{12}\text{C}/^{13}\text{C}$ ratio

Li-abundances for the program stars were determined by synthesizing the resonance doublet at 6707 \AA and the abundances are provided in the table 3. We did not detect any distinguishable spec-

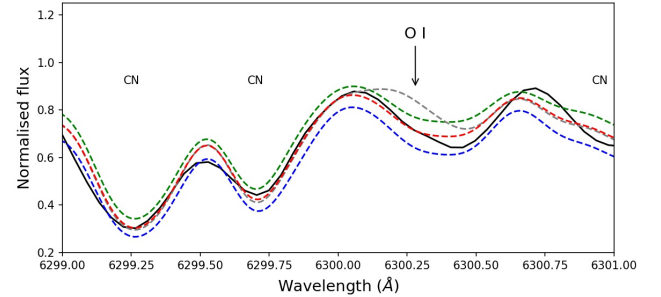


Figure 2. The [OI] line at 6300.3 \AA is fitted with synthetic spectra of different abundances. The black solid line is the observed spectrum of HE 0017+0055 and the red spectrum is the best fit which corresponds to $[O/Fe] = 0.7$ dex. The green and blue spectra denote the syntheses corresponding to the range of uncertainty of ± 0.3 dex in oxygen abundance. The grey synthetic spectrum corresponds to the case where [O I] line has been removed from the line list.

tral features of Li in the region, thus, we only derived an upper limit for the abundances. Due to the heavy contamination from CN molecular features to the Li line, we assigned an uncertainty of 0.3 dex to the derived values. Since all the samples in the study are in the giant phase, the low values for $A(\text{Li})$ ⁵ are consistent with their evolutionary phase. During the RGB evolutionary stage, the surface Li is taken into the deeper interiors through convective mixing where it is easily destroyed due to the high interior temperatures (Gratton

⁵ $A(X) = \log \epsilon(X) = \log (N_X/N_H) + 12$, where N_X and N_H represent number densities of a given element X and hydrogen respectively.

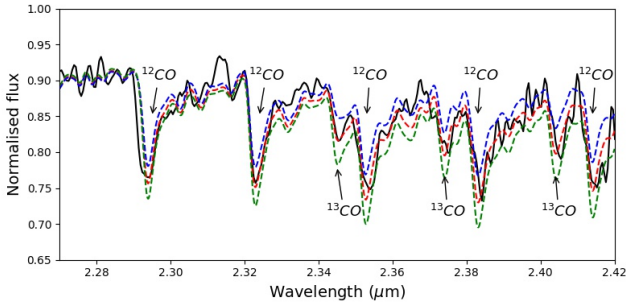


Figure 3. The NIR CO molecular bands are fitted with various synthetic spectra. The black solid line represent the observed spectrum of HE 0017+0055. The red spectrum is the best fit to the observed spectrum which corresponds to $[C/Fe] = 2.1$ and $[O/Fe] = 0.6$. The green and blue spectra indicate syntheses corresponding to the range of uncertainty of ± 0.3 dex in oxygen abundance.

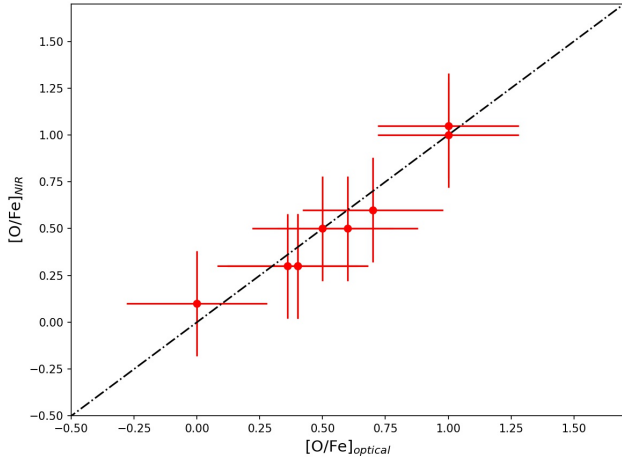


Figure 4. The oxygen abundances derived from optical and NIR spectra have been compared. The abundances are matching within an error of 0.3 dex. The black dotted dashed line corresponds to the points where the oxygen abundances from NIR and optical spectral lines are identical.

et al. 2000; Lind et al. 2009). To confirm the mixing scenario, we compared the Li abundances of our program stars with the objects from Spite et al. (2005) and Sbordone et al. (2010) in the figure 5 and identified that all the program stars occupy the same region as that of the mixed giants.

The $^{12}C/^{13}C$ ratio was calculated using the NIR ^{12}CO and ^{13}CO molecular band heads at $2.38 \mu m$ (refer figure 3). We have also derived the carbon isotopic ratio from $^{12}C_2$ and $^{12}C^{13}C$ band heads at 4737 and 4744 \AA respectively (refer figure 6) to check the consistency of the values derived from low-resolution NIR spectra. We assign an uncertainty of 6 to the $^{12}C/^{13}C$ ratio measurements, below which the variation in the ratio could not be detected with the goodness of fit. When comparing, we found that the $^{12}C/^{13}C$ ratios from optical spectra are matching with that derived from the NIR ^{12}CO and ^{13}CO molecular bands and compared these in the figure 7. The ratios derived from optical and NIR spectra are mentioned in table 5.

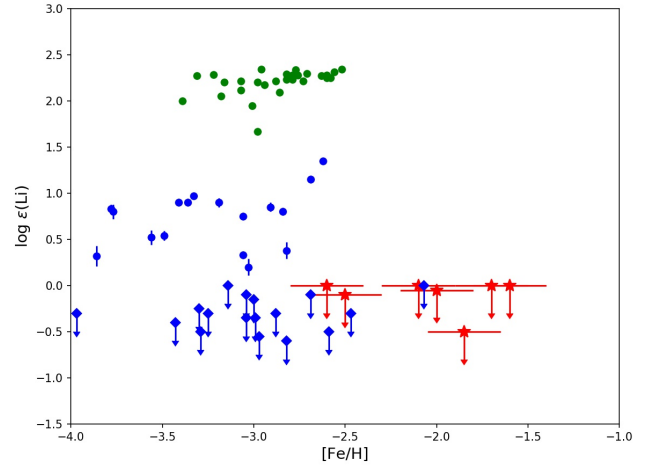


Figure 5. The Li abundance of our program stars (red star symbols) is compared with the Li abundance of C-normal stars from the literature. The filled circles correspond to unmixed stars from Sbordone et al. (2010) (green, main-sequence turnoff and dwarf stars) and Spite et al. (2005) (blue, early RGB) whereas the blue diamond symbols correspond to the mixed giants from Spite et al. (2005). The Li abundance of our program stars occupy the same region as that of the mixed giants.

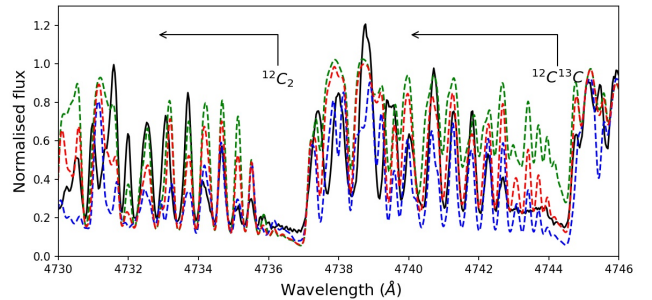


Figure 6. The $^{12}C_2$ and $^{12}C^{13}C$ molecular features of HE 0017+0055 are plotted as black spectrum. The bandheads at 4737 and 4744 \AA are marked with arrows indicating the direction at which the corresponding molecular features are present. From the figure, it can be seen that the red spectrum is the best fit and it corresponds to a $^{12}C/^{13}C = 9$. The blue spectrum corresponds to $^{12}C/^{13}C = 2$ whereas the green spectrum corresponds to $^{12}C/^{13}C = 99$.

4.4 α -elements and odd Z elements

Among the α -elements, we derived the abundances of Mg and Ca. The Mg I triplet lines at 5172 \AA and 5183 \AA lines are very strong so we did not use them to derive the Mg abundance. Instead, we have used the 5528 \AA and 5711 \AA to derive the abundances, in particular, we have used 5711 \AA for the abundance measurements only if the line is identified to be free from blending. The NLTE corrections for these lines are either negligible or not available for the parameter set of our program stars (Lind et al. 2011; Bergemann et al. 2017a,b). We have used four Ca I lines, whichever are free of blending with molecular features, to derive the Ca abundance. The median of the abundances from individual lines is calculated and provided in the table 3.

Among the odd Z elements, we derived the abundances of Na,

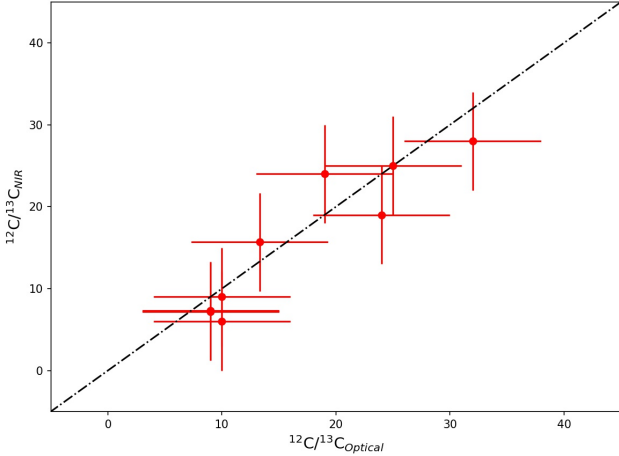


Figure 7. The carbon isotopic ratio derived from optical and NIR spectra are compared here. The black dotted dashed line corresponds to the points where the $^{12}\text{C}/^{13}\text{C}$ from NIR and optical spectral lines are identical.

Al, K and Sc using the high resolution spectra and the details of the lines are given in the table A1. The Na D lines were not used as the lines are too strong for deriving the abundances. So we depended on the weaker lines 5682 Å and 5688 Å to derive the Na abundance. The NLTE corrections for these Na I lines were performed from Lind et al. (2011) whenever available and the average values are listed in the table 3. Al I lines at 6696 and 6698 are used for deriving the Al abundance and these lines have negligible contributions from NLTE effects (Baumueller & Gehren 1997; Nordlander & Lind 2017). For the case of K, whenever the feature at 7698.98 Å has contributions from telluric features, the abundance from 7664.87 Å is quoted, otherwise the average of the abundances from both the lines is quoted in table 3. Both these lines are sensitive to NLTE effects (Takeda et al. 2002; Kobayashi et al. 2006; Andrievsky et al. 2010; Prantzos et al. 2018; Reggiani et al. 2019) and the NLTE corrections depend on the effective temperature and surface gravity of the model. Using the NLTE grid provided in Reggiani et al. (2019), we have estimated the NLTE corrections for the program stars and the NLTE corrected values are given in the table 3. The NLTE grid does not cover very low log g values, so we could not estimate the NLTE corrections for HE 1152-0355 and HE 0314-0143. We could not measure the K abundance in HD 5223 due to the contamination from telluric features. For the case of Sc abundance, we could not find any study of Sc line formation in NLTE except in Zhang et al. (2008) where they have studied the NLTE effects only for the sun and identified negligible NLTE effects for Sc II lines. So we report only LTE results for this element in the table 3. The resolution of the NIR spectra was too low to resolve the HF feature from the nearby features, so we could not derive F abundance in these stars.

The spectral features of the Fe-peak elements are severely blended with the molecular features of C and N to derive any meaningful abundances. So we could not make any reliable measurements of their abundances.

Table 5. The oxygen and carbon isotopic ratio from NIR and optical spectra.

star name	[O/Fe]		$^{12}\text{C}/^{13}\text{C}$	
	Optical	NIR	Optical	NIR
HD 5223	0.4	0.3	25	25
HE 1152-0355	0.5	0.5	10	9
HE 1418+0150	1.0	1.0	9	7
BD+42 2173	0.4	0.3	39	32
HD 187216	0.0	0.1	10	6
HE 0017+0055	0.7	0.6	9	7
HE 0314-0143	1.0	1.1	13	16
BD+41 2150	0.6	0.5	24	19
C* 782	0.4	0.3	32	28

4.5 Neutron capture elements

We derived the abundances of light s -process elements (ls: Y, Zr) as well as heavy s -process elements (hs: Ba, La, Nd, Ce, Pr,) and r -process elements (Eu and Sm) to understand the origin of neutron-capture elements using various spectral lines in the high-resolution optical spectrum. The [hs/ls]⁶ ratio of all the program stars are provided in the table 3. The CN band head at 4215 Å is saturated in all our program stars. So the abundance of Sr could not be measured from the Sr II resonance line at 4216 Å. The details of the lines used for the abundance measurements are given in the table A1. For the case of Rb abundance, we have quoted the abundance from the Rb I line at 7800.2 Å and we did not use the 7947.5 Å line since it was severely blended with the CN molecular feature. For Ba and Eu, we used the Ba II lines at 5853 Å and 6141 Å and Eu II line at 6645 Å for the abundance determination. We checked for available NLTE corrections to these features and identified to have negligible contributions from NLTE effects (Mashonkina et al. 1999; Mashonkina & Gehren 2000; Mashonkina & Christlieb 2014; Gallagher et al. 2020).

4.6 Oxygen abundance of the program stars

We derived the oxygen abundance of 9 carbon enhanced stars using both optical and NIR spectra. The oxygen abundances of HD 5223, HD 187216, BD+42 2173 and C*782 are not available so far in the literature. For the case of HE 1152-0355, HE 1418+0150, HE 0017+0055 and HE 0314-0143; Kennedy et al. (2011) had reported the oxygen abundances from the low-resolution NIR CO lines. Using low-resolution NIR and high resolution optical observations, we confirm the O abundances in these stars. The abundances are given in table 5. The stellar parameters and abundance details of C*782 and BD+41 2150 are not discussed elsewhere in the paper as their abundance pattern was found to be more complex and does not fit in the theme of this paper. So we confine the results from these two stars to the oxygen abundance and their carbon isotopic ratio. A detailed abundance analysis of the two objects will be discussed in an upcoming paper, Susmitha *et al.* (in prep).

⁶ This ratio defines the enrichment of the second peak of the s -process (hs), with respect to the first peak, light s -process (ls) elements. It is defined as [hs/ls] = [hs/Fe] - [ls/Fe] in the usual spectroscopic notation. We adopt [ls/Fe] = [Y+Zr/Fe]/2 and [hs/Fe] = [Ba+La+Ce/Fe]/3.

4.7 Comparison with literature

Since our program stars were chosen from the literature, we compare the stellar parameters and various elemental abundances with the previous studies .

HD5223: This program star was studied by [Goswami et al. \(2006\)](#) and classified as a CEMP-*s* star based on the abundances from Ba, La and Ce. The derived stellar parameters from their study and from our study are matching within the error quoted in sec. 4.1. But the classification of HD 5223 as CEMP-*s* stars is revisited here and classified it as CEMP-*r/s* using the [Eu/Fe] abundances which was not done in the earlier studies.

HE 1152-0355: [Goswami et al. \(2006\)](#) have reported the stellar parameters and classified the star as a CEMP-*s* star. [Kennedy et al. \(2011\)](#) have re-derived the stellar parameters and obtained the C and O abundances. Our stellar parameters and C and O abundances are also matching with the values from [Kennedy et al. \(2011\)](#) within the uncertainties quoted in table 3.

HE 1418+0150: [Kennedy et al. \(2011\)](#) have reported the stellar parameters and C and O abundances using low-resolution spectra. We derived the stellar parameters and abundances using high resolution spectra and obtained a larger $\log g$ and slightly higher metallicity (refer table 2). [Hansen et al. \(2016c\)](#) has derived the Sr and Ba abundances of this star and classified them as MP(*s*). The abundances of rest of the neutron-capture elements in this star and their nucleosynthetic origin were not reported earlier. We classify the star as CEMP-*r/s* using the [Eu/Fe] and [Ba/Fe] values.

HD 187216: [Kipper & Jorgensen \(1994\)](#) reported this star as a possible intrinsic AGB star due to the high carbon and *s*-process element abundances with a low $\log g$ value and the non-detection of a binary companion. [Jorissen et al. \(2016a\)](#) monitored the radial velocity and confirmed the binary nature with a period longer than 10^4 days. We classify this stars as CEMP-*r/s* star based on the abundances of Ba and Eu.

HE 0017+0055: This star was identified as a CEMP-*r/s* star using the excess abundance of C and *s*-process and *r*-process elements and radial velocity variations with a period of 384 days ([Jorissen et al. 2016a,b](#)). [Kennedy et al. \(2011\)](#) derived the O abundance in the star using NIR CO lines. Our stellar parameters and the various elemental abundances are also inline with the estimates from [Kennedy et al. \(2011\)](#) and [Jorissen et al. \(2016b\)](#).

HE 0314-0143: [Kennedy et al. \(2011\)](#) derived the stellar parameters, C and O abundances from low-resolution spectra. In the literature, this star was not classified into any sub category of carbon enhanced stars as no high-resolution observations were available. We classify this star as CEMP-*r/s* based on the neutron-capture elemental abundances.

BD+42 2173: [McClure & Woodsworth \(1990\)](#) identified this star showing radial velocity variations with a period of 328 days. [Aoki & Tsuji \(1997\)](#) reported lower $^{12}\text{C}/^{13}\text{C}$ value whereas we have obtained a slightly higher value for $^{12}\text{C}/^{13}\text{C}$ ratio which is given in table 5.

5 DISCUSSION

We studied the abundance pattern of 7 CEMP stars using optical and NIR spectroscopy. These stars exhibit high carbon abundance. [Spite et al. \(2013\)](#); [Bonifacio et al. \(2015\)](#); [Hansen et al. \(2015\)](#), and [Yoon et al. \(2016\)](#) identified the existence of bimodality in the distribution of A(C) for CEMP stars where most of the CEMP-*s* stars populate the high-C band whereas most of the CEMP-*no* stars

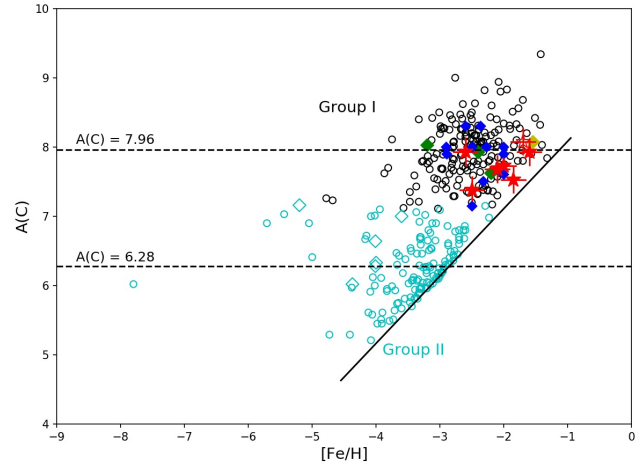


Figure 8. The C abundance of CEMP stars from [Yoon et al. \(2016, & references therein\)](#) is plotted as open circles in which the CEMP-*s* and -*r/s* stars are plotted as black open circles whereas the CEMP-*no* stars are plotted as cyan open circles. The filled symbols represent the C abundance of CEMP-*r/s* stars from various studies including [Hansen et al. \(2019b\)](#), green diamonds, [Sbordone et al. \(2020\)](#), yellow diamond) and [Karinkuzhi et al. \(2021\)](#), blue diamonds). The red star symbols correspond to the C abundances of stars from this study. The cyan open diamond symbols represent the C abundance of stars from [Bonifacio et al. \(2018\)](#). The black solid line corresponds to [C/Fe] = +0.7. The horizontal dashed lines represent the high and low C band according to [Yoon et al. \(2016\)](#). The CEMP-*r/s* stars are identified to be scattered in the high C band region.

populate the low-C band. We compared the C abundance of our program stars with the CEMP stars from the literature ([Yoon et al. 2016](#); [Bonifacio et al. 2018](#); [Hansen et al. 2019b](#); [Sbordone et al. 2020](#); [Karinkuzhi et al. 2021](#), & references therein) to check any peculiar abundance trend is associated with CEMP-*r/s* subcategory (refer figure 8). From the figure, it can be seen that the C abundance of CEMP-*r/s* stars populate the high-C band region in the A(C) vs [Fe/H] space. While the A(C)-[Fe/H] diagram is useful in separating the CEMP-*no* stars from other CEMP subclasses, it is not efficient in separating CEMP-*r/s* stars from CEMP-*s* sub-category. The program stars also exhibit enhancement in the neutron-capture elements. The radial velocities measured from the current optical spectra and the literature values, show variations indicating the possibility of the program stars to be in a binary system. The enhancement in carbon along with the neutron-capture elements and radial velocity variations favor AGB mass transfer star as a possible mechanism for the enhanced carbon and n-capture elements. The extrinsic origin of C is further supported by the location of A(C) of these stars in the A(C)- [Fe/H] diagram. The abundance pattern exhibited by the CEMP stars provide clues about AGB nucleosynthesis at such low-metallicities. Here, we use the n-capture elements to understand the AGB nucleosynthesis and various mixing processes that will bring the carbon and neutron rich nuclei to the surface, while the abundance of light elements such as C,N,O and Na can be used to constrain the mass of the companion. So we divide the discussion into two parts. In the first part, we will show how the abundance of light elements such as C, N, O and Na can be used to constrain the mass of the companion AGB star and in the second part, we will discuss how the neutron capture elements can provide details of the inter-shell mixing and nucleosynthesis processes.

5.1 C,N,O and Na to constrain the AGB mass

The abundance pattern of C, N, O, and Na of our program stars, when compared with the models of AGB stars, indicate abundance trend with that of a low-mass AGB stars than higher mass AGB stars (refer figure 9). It can be seen that while the trend of observed abundance matches with that of the models, the observed abundance values are different from the model values. Several factors contribute to this difference including the nucleosynthesis and mixing in the AGB star, the mass of the accreted matter, mixing and dilution of accreted matter on the surface of the CEMP star etc. Since our program stars are all in the giant phase, the accreted matter would have experienced dilution and mixing of processed material from the deeper layers. The observed abundances are not corrected for any such mixing and dilution. The inclusion of mixing and dilution could alter the [C/N] ratios. According to Stancliffe et al. (2009), the observed C and N abundances among the CEMP giants are sensitive to the mass of the C-rich material accreted from the AGB companion. So the details of accreted mass are required to do the corrections. Hence, a direct comparison of the observed abundances with theoretical models is not performed here to constrain the actual mass of the AGB star instead we restrict our comparison to the trend of abundance distribution. The observed Na abundances of the sample is also consistent with low mass AGB contribution (refer figure 10).

While there is an overall agreement to the trend of these elements, a discrepancy is found in the $^{12}\text{C}/^{13}\text{C}$ values. According to low-mass AGB models, the $^{12}\text{C}/^{13}\text{C}$ should be very high upto $\log(^{12}\text{C}/^{13}\text{C}) = 3.4$ for AGB stars of mass $M < 3M_{\odot}$ (Fishlock et al. 2014) so the observed high ^{12}C in the CEMP stars is considered to be due to the mass transfer from a low-mass AGB companion. More massive AGB models ($M > 3M_{\odot}$) produce low carbon isotopic ratio ($\log(^{12}\text{C}/^{13}\text{C}) < 2.0$) through Hot Bottom Burning (HBB), a process that happens at the bottom of the convective envelope which converts carbon to nitrogen when the temperature is sufficient for CN cycle. The values of carbon isotopic ratio thus obtained are similar to the values observed in CEMP stars. However, such massive companion stars also produce high nitrogen abundance resulting in $[\text{C}/\text{N}] < 0$. HBB also results in the production of lighter *s*-process elements than heavy *s*-process elements resulting in $[\text{hs}/\text{ls}] < 0$ which is not found in any of the stars studied here. This makes HBB an unlikely scenario for the observed low carbon isotopic ratios.

All the program stars in this study are giants and they would have undergone several mixing episodes during the first dredge-up, thermohaline mixing, extra mixing for the RGB bump, etc (Charbonnel et al. 1998; Stancliffe et al. 2007; Smiljanic et al. 2009). This changes the surface composition of the carbon and carbon isotopes that was originally accreted from the AGB companion and would finally result in an intermediate nitrogen enhancement (still $[\text{C}/\text{N}] > 0.1$) as well as the low isotopic ratio (Proffitt & Michaud 1989; Barbay et al. 1992; Keller et al. 2001; Denissenkov & Pinsonneault 2008) (refer figure 11). While the mixing in the CEMP star is put forward as one of the reasons for the low $^{12}\text{C}/^{13}\text{C}$ ratio, the CEMP stars in main-sequence or turn-off stage are also identified to be showing low carbon isotopic ratios (Aoki et al. 2002; Lucatello et al. 2003; Masseron et al. 2010). So the measured low $^{12}\text{C}/^{13}\text{C}$ ratio could be the resultant of some extra mixing in the companion AGB star itself.

The concept of Cool Bottom Processing (CBP) can also be invoked to explain the moderately high nitrogen abundance and low $^{12}\text{C}/^{13}\text{C}$. In CBP, the material from the base of the convective envelope is mixed into the radiative region located on top of the H-burning

shell where material captures protons and then brought back to the envelope thereby leaving CN processed materials at the surface of the star (Wasserburg et al. 1995). Nitrogen and ^{13}C are being the byproducts of the CN cycle, a complete CN cycle produces $^{12}\text{C}/^{13}\text{C} \sim 4$ and $[\text{C}/\text{N}] \sim -1.3$. Thus the observed low $^{12}\text{C}/^{13}\text{C}$ and $[\text{C}/\text{N}]$ values can be obtained when the carbon is partially processed possibly in the H-burning shell before reaching the convective envelope. Such a mechanism could explain the moderately high nitrogen abundance and low carbon isotopic ratio observed in CEMP stars. CBP is hypothesized to occur in the RGB phase of stars having $M \leq 2.5M_{\odot}$ (Charbonnel 1995) and in AGB stars where an extra mixing happens at the bottom of the AGB envelope, and a part of this envelope material turns carbon into nitrogen through CN cycle (Nollett et al. 2003; Lugaro et al. 2017). Though the physical mechanism causing the CBP is unclear, an extra mixing process is required to explain the observed abundances, which include the instabilities generated due to the molecular weight inversion induced by ^3He burning (Eggleton et al. 2008) and the magnetic buoyancy induced by a stellar dynamo (Busso et al. 2007; Palmerini et al. 2008).

For the case of oxygen abundance, low-metallicity AGB stars are expected to produce an elevated oxygen abundance from $^{12}\text{C}(\alpha, \gamma)^{16}\text{O}$ reaction activated due to the hotter conditions in the helium burning shell. But the oxygen yields predicted by different models do not agree with each other. Herwig (2004) find that the oxygen abundance decreases with mass of the AGB star due to the dilution in the AGB envelope. Though the dredge up matter brings more oxygen to the surface, the dilution dominates the dredge up when the mass increases. Karakas & Lattanzio (2007) found a contradicting scenario. According to their models, as the mass increases, in the He shell, the reaction $^{12}\text{C}(\alpha, \gamma)^{16}\text{O}$ is favored by the competition between the dilution and the hotter conditions and around $3M_{\odot}$, maximum oxygen yield is predicted. All the models assume a solar scaled abundance for the key elements to start with. The amount of the elements produced during AGB evolution is so high that the initial assumptions do not affect the final composition. In contrary, the oxygen is produced in the scale of $[\text{O}/\text{Fe}] \sim 0.5$ in metal-poor stars (Lucatello et al. 2011) which is greatly influenced by the initial composition.

Another scenario which can account for observed CNO abundance, especially the low carbon isotopic ratio and moderately high nitrogen abundance, is the Proton Ingestion Episodes (PIEs). At the beginning of the thermally pulsating phase of low-mass low-metallicity AGB stars, the convective envelope extends up to the base of the H-rich envelope and the protons get mixed in to the convective shell which are captured by ^{12}C . This produces ^{13}C and ^{14}N through various reactions which results in a deep-Third Dredge Up (TDU). After the deep TDU, the model follows the standard AGB evolution. Each thermal pulses bring the synthesized material to the surface of the stellar envelope resulting in constantly varying the surface composition. The observed high ^{13}C is also produced in the PIE. The final abundance pattern at each TDU phases resembles to the CNO abundance pattern exhibited by the stars in this study (refer figures 6 and 7 in Cristallo et al. (2009). Regardless of the abundance pattern exhibited, certain uncertainties are also associated with the PIEs. Enhancement in the alpha elements can suppress the PIEs as the proton ingestion requires lower CNO abundance to break the entropy barrier. Also the mixing and nucleosynthetic mechanisms in the convective regions do not account for the assumptions of mixing length theory and one dimensional spherically symmetric evolution (Cristallo et al. 2009; Herwig et al. 2011). Nevertheless, we can

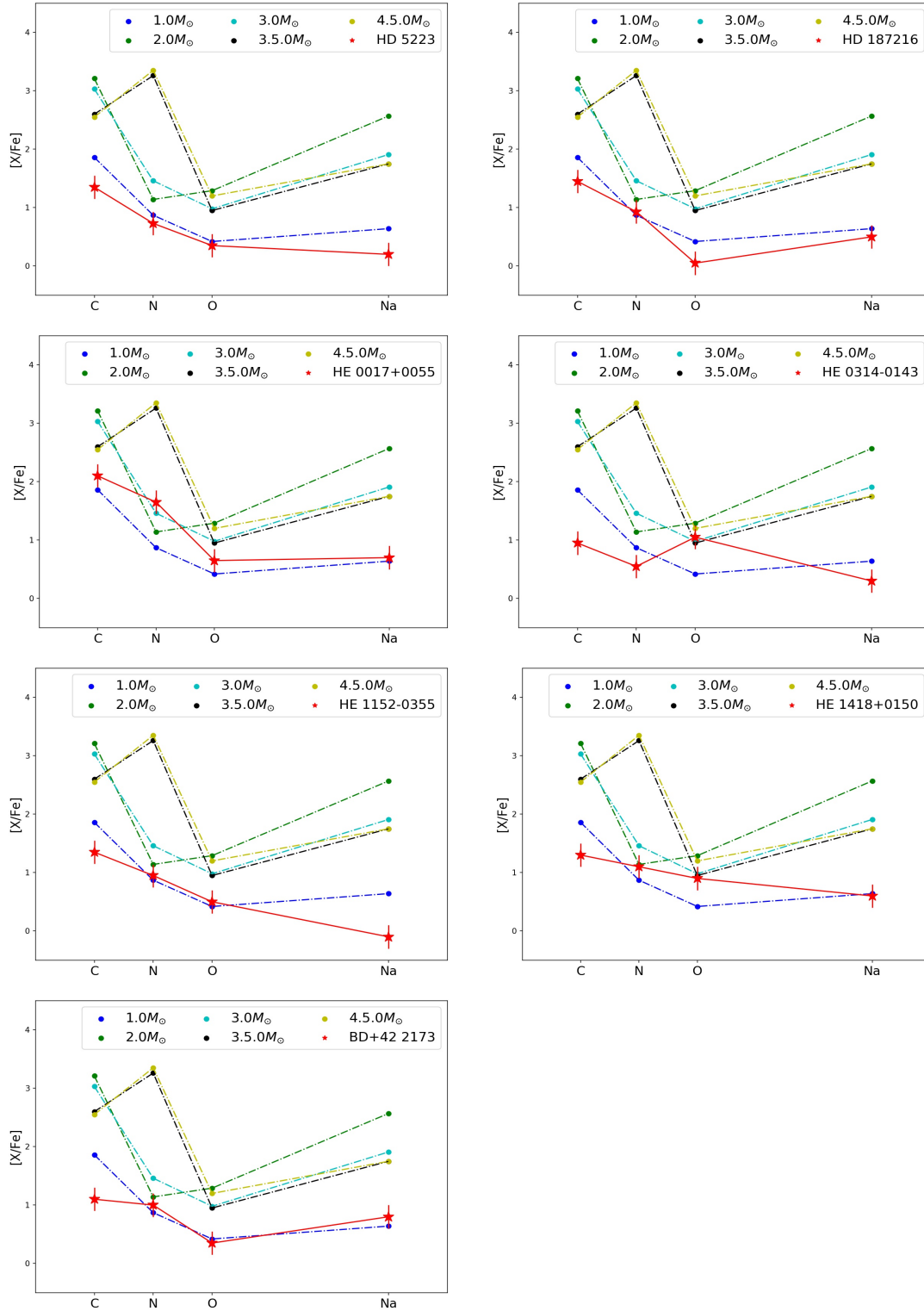


Figure 9. The observed CNO and Na(LTE) abundances of the program stars and the abundances from the standard AGB models of different masses (Lugaro et al. 2012) are plotted. The observed values are not corrected for the dilution and mixing of CN processed material in the CEMP star. However, it can be seen that the trend of the abundance distribution of the observed stars resembles with that of low-mass AGB stars ($M \leq 3M_{\odot}$). For the case of HE 0314-0143, (which has the lowest temperature, lowest $\log g$ among the program stars), the poor match between the observed values and models could be due to some extra mixing during the evolution which would result in a larger depletion of C.

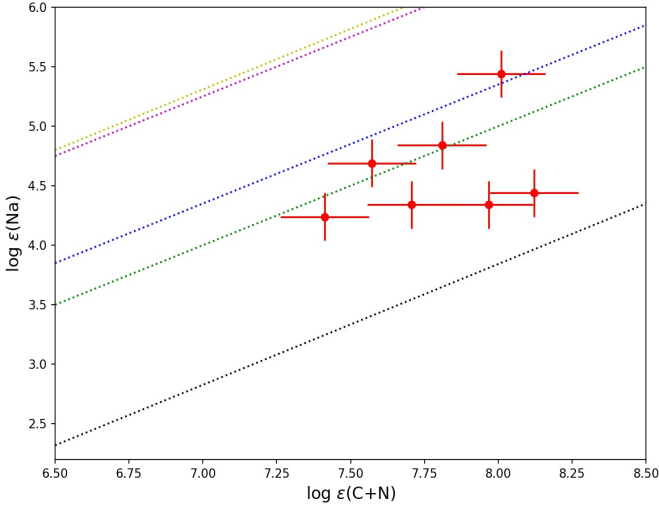


Figure 10. The absolute Na abundances (LTE) of our program stars are plotted as a function of the absolute (C+N) abundances. The dotted lines represent the abundances corresponding to AGB models from Karakas & Lattanzio (2007) for different masses: the black dotted line corresponds to the AGB model of $1.25M_{\odot}$, the green dotted line corresponds to $1.75M_{\odot}$, the blue dotted line corresponds to $2.5M_{\odot}$, the magenta dotted line corresponds to $3.0M_{\odot}$ and the yellow dotted line corresponds to $3.5M_{\odot}$ AGB model. This figure is inspired from figure 10 in Lucatello et al. (2011).

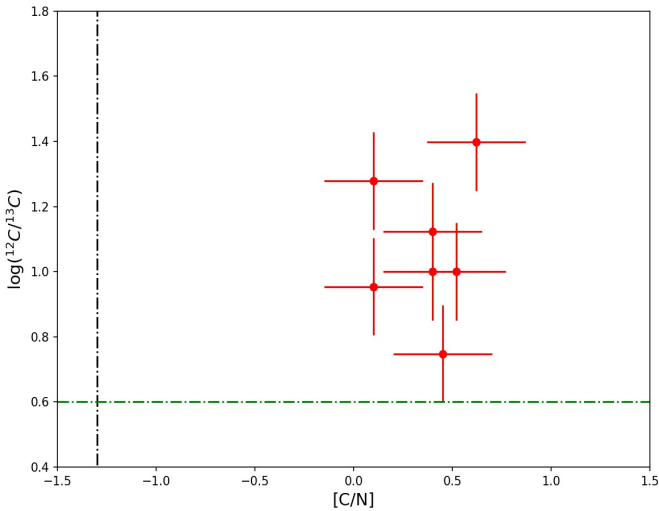


Figure 11. The $^{12}\text{C}/^{13}\text{C}$ ratio of our program stars are plotted as a function of $[\text{C}/\text{N}]$. The dashed lines represent the values for a complete CN cycle where $[\text{C}/\text{N}] \sim -1.3$ and $^{12}\text{C}/^{13}\text{C} \sim 4$. While the low-mass AGB models ($M < 3.0M_{\odot}$) predict $\log(^{12}\text{C}/^{13}\text{C})$ upto 3.4, more massive AGB models predict $\log(^{12}\text{C}/^{13}\text{C})$ as low as 0.6 due to HBB. Although the low values of $^{12}\text{C}/^{13}\text{C}$ of our program stars are similar to the model prediction of HBB, the observed $[\text{C}/\text{N}]$ values and $[\text{h}/\text{s}]$ ratios of our program stars rule out HBB as a likely scenario for the enrichment of ^{13}C and N. So the observed values of $^{12}\text{C}/^{13}\text{C}$ and $[\text{C}/\text{N}]$ could be the resultant of either thermohaline mixing, extra-mixing during first dredge-up, extra mixing for the RGB bump or the extra mixing in the companion AGB star itself.

associate the PIEs with a few TDUs contributing to the observed CNO abundances and low isotopic ratio in CEMP stars.

5.2 Neutron capture elements to constrain the nucleosyntheses in the companion AGB star

All the program stars in this study are rich in both s -process and r -process elements. Among the program stars, HE 1152-0355 satisfies the criteria to be classified as a CEMP- s star. So the abundance pattern of this star is compared with that from low-mass AGB models. We compared the AGB models from F.R.U.T.Y (Full-network repository of Updated Isotopic Tables & Yields) database (Cristallo et al. 2011) where we chose models comparable to the metallicity of HE 1152-0355. $[\text{Rb}/\text{Zr}]$ being an important tracer for the mass of the companion AGB stars in CEMP- s population, we use the $[\text{Rb}/\text{Zr}]$ ratio of the star to constrain the masses of the models. Since the star exhibits a low $[\text{Rb}/\text{Zr}]$ ratio ($[\text{Rb}/\text{Zr}] < -0.7$), we restricted the comparison to only low-mass models which is also consistent with the results from the section 5.1. The fitting is done with the available models ($1.5M_{\odot}$, $2M_{\odot}$, $3M_{\odot}$) in the database and is shown in the figure 12. All these models exhibit similar distribution for most of the elements and the abundances of hs -elements in HE 1152-0355 matches with all the model values within the uncertainty. Since we do not have the information of mixing and dilution on the surface of the CEMP star and the efficiency of mass-transfer from the companion AGB star, we restrict our analysis to comparing the model values with the observed ones instead of addressing the reasons behind the difference in various abundances with the model predicted values. Except HE 1152-0355, all the stars have $[\text{Ba}/\text{Fe}] > 1.0$, $[\text{Eu}/\text{Fe}] > 1.0$ and $[\text{Ba}/\text{Eu}] > 0$ (refer figure 13). Thus we classify these stars as CEMP- r/s . (refer table 2).

Various theories have been put forward to explain the origin of both s - and r -process elements in CEMP- r/s stars. Eu being the r -process representative (Beers & Christlieb 2005), its enhancement along with the enhancement in Ba, the s -process representative (Lugaro et al. 2012). While the s -process requires neutron densities, $n \approx 10^6 - 10^{10} \text{ cm}^{-3}$ (Busso et al. 1999), the r -process requires n higher than 10^{20} cm^{-3} (Goriely et al. 2005; Thielemann et al. 2011). So different formation sites have been proposed to explain the origin of these elements. In which, the carbon and s -process elements originate from the AGB companion similar to that in CEMP- s stars where the birth cloud of the binary system was previously enriched with the r -process elements from supernovae explosions and/or neutron star mergers (Bisterzo et al. 2012).

Recent computations explored an intermediate neutron densities to s - and r -processes and they were successful in producing the abundance patterns of CEMP- r/s stars (Hampel et al. 2016; Denissenkov et al. 2017). The neutron-capture process in this intermediate neutron density ($\sim 10^{15} \text{ cm}^{-3}$) is called as i -process and is activated by the rapid ingestion of a significant amount of H in He-burning convective regions (Cowan & Rose 1977). Even though the nucleosynthetic sites for i -process is still a debate, the proposed sites include: low-mass, low-metallicity AGB stars (Campbell & Lattanzio 2008; Campbell et al. 2010; Cruz et al. 2013; Cristallo et al. 2016), super-AGB stars (Doherty et al. 2015; Jones et al. 2016), evolved low-mass stars (Herwig et al. 2011; Hampel et al. 2016, 2019), rapidly accreting white dwarfs (RAWD) in closed binary systems (Herwig et al. 2014; Denissenkov et al. 2017) and massive metal-poor stars (Banerjee et al. 2018; Clarkson et al. 2018).

We compared the neutron-capture elemental abundance pattern of our program stars with available i -process models of similar metal-

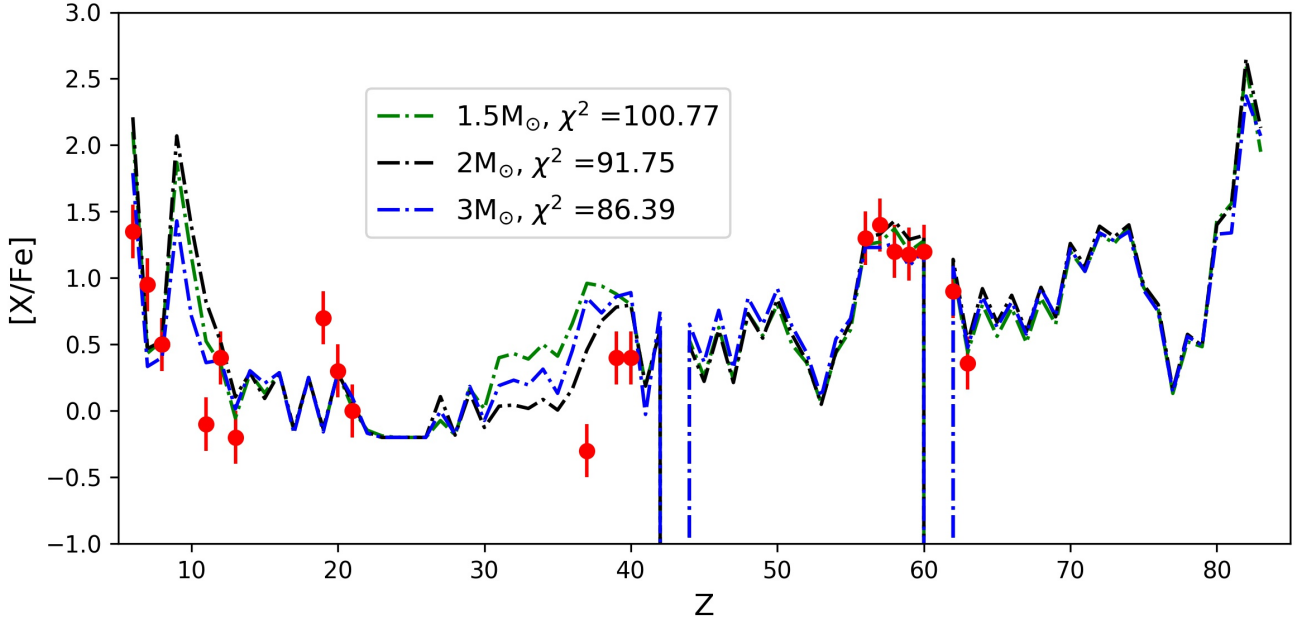


Figure 12. Various elemental abundances of the CEMP-*s* star, HE 1152-0355 (red filled circles), are fitted with AGB models of different masses. The abundance pattern for different masses and the respective chi-square values are listed in the legend

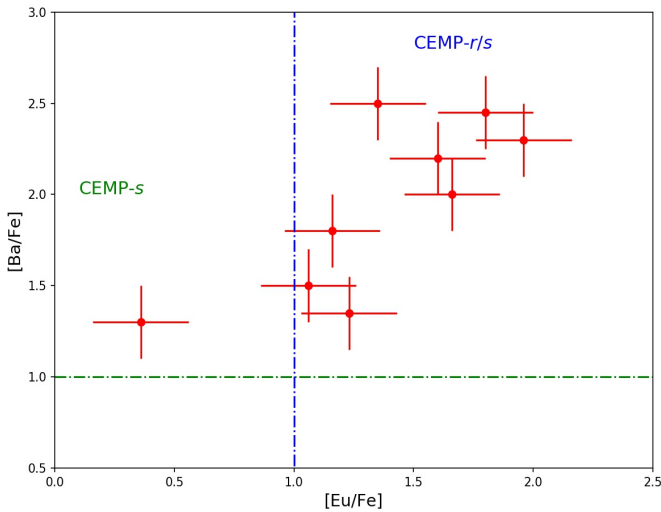


Figure 13. The [Ba/Fe] and [Eu/Fe] of all program stars are plotted here. The region of various CEMP population is marked in the figure. The region where [Ba/Fe] > 1.0 and [Eu/Fe] > 1.0 is where the CEMP-*r/s* population occupies whereas the CEMP-*s* population fills the region where [Ba/Fe] > 1.0 and [Eu/Fe] < 1.0.

licity (Hampel et al. 2016; Denissenkov et al. 2019). The figure 11 and 12 in Denissenkov et al. (2019) predicts over enhancement for neutron-capture elements than the observationally derived values for our program stars. So the abundances are not matching with the RAWD models values (Denissenkov et al. 2019) whereas for the case of Hampel et al. (2016) models, we find a good agreement (refer figure 14). As explained in the sec 5.1, at the bottom of the

convective envelope, the ^{13}C produced in PIEs acts as a source of neutrons through $^{13}\text{C}(\alpha, n)^{16}\text{O}$ reaction. These PIEs can produce necessary neutron densities as large as 10^{15} cm^{-3} (Cristallo et al. 2009). We have only considered elements $37 \leq Z \leq 63$ since the model is available only for elements heavier than Fe. We used the equation given in Hampel et al. (2016) to calculate the model abundance on the surface of the CEMP-*r/s* stars:

$$X = X_i * (1 - d) + X_{\odot} * d$$

where X_i is the calculated *i*-process abundance of each element from the model, X_{\odot} is the scaled-solar abundance, and *d* the dilution factor, which provides the measure of how much *i*-processed material is mixed with unprocessed material. However, the dilution factor in this equation does not provide any quantitative measure on various specific mixing mechanisms on the AGB surface or mass-transfer onto the CEMP star (Hampel et al. 2019), instead it is a free parameter and is varied until we obtain a best-fitting for a model and the observed abundances for different neutron densities. Since the dilution factor does not have any physical significance, we are not quoting the value. The best-fit is calculated using the equation:

$$\chi^2 = \sum_{Z=37}^{63} \frac{[X_Z/Fe]_{obs} - [X_Z/Fe]_{mod}}{\sigma_{Z,obs}^2}$$

Where $\sigma_{Z,obs}^2$ is the observational error of $[X_Z/Fe]_{obs}$ and $[X_Z/Fe]_{obs}$ and $[X_Z/Fe]_{mod}$ are observed and model abundances of the element with atomic number *Z*. χ^2 indicates the goodness of the fit to tell which model matches the observations best, but its value does not have the statistical meaning in the conventional sense. The best fit model parameters and the corresponding χ^2 is mentioned in each plot for all the program stars (refer figure 14).

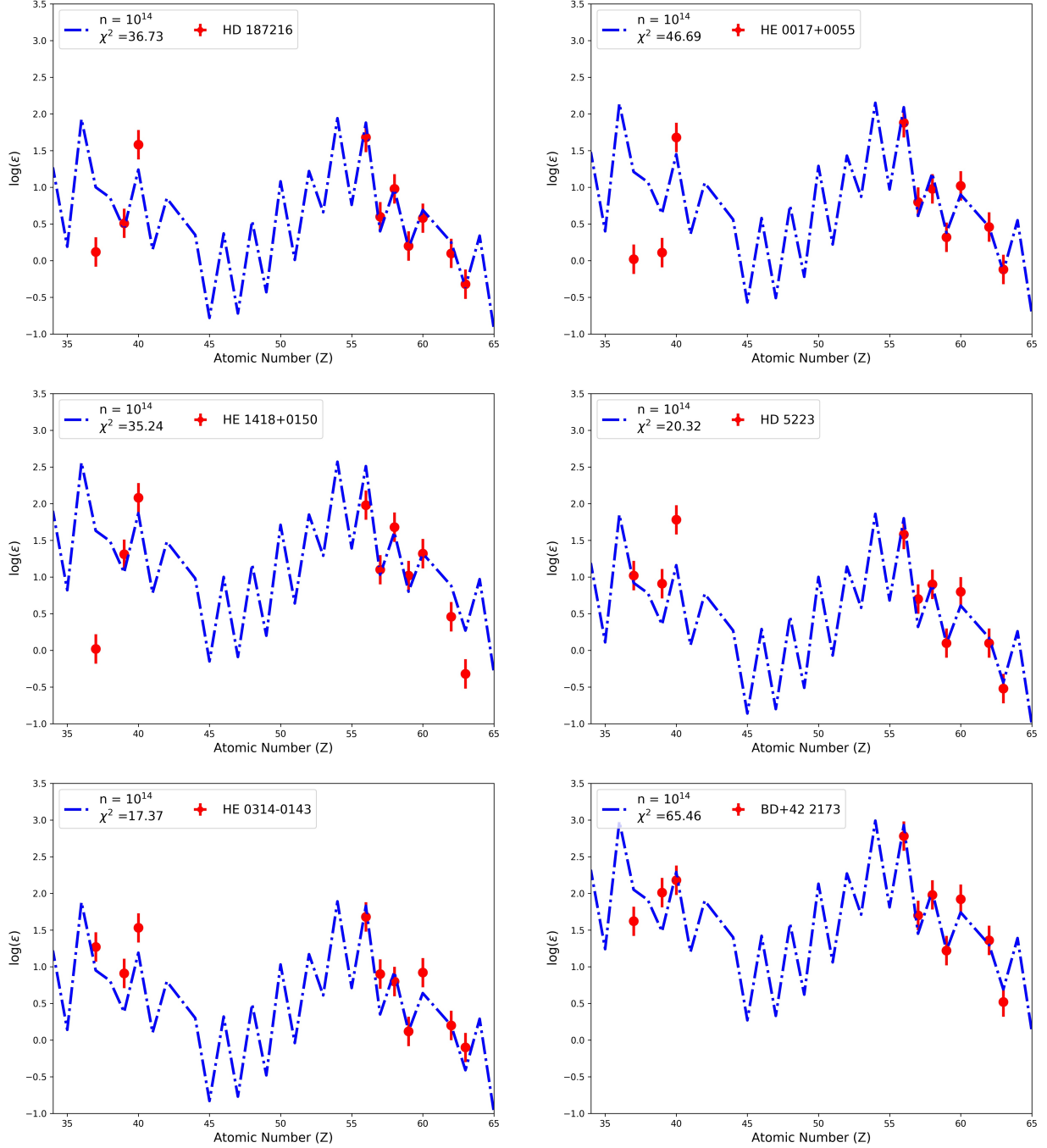


Figure 14. The CEMP-*i* models from Hampel et al. (2016) is fitted with the heavy elemental abundance of stars from this study.

The models from Hampel et al. (2016) provide a fairly good match with the observed data. However, the authors have noted that the neutron-capture processes considered in Hampel et al. (2016) use one-dimensional single-zone nuclear-network calculations without clearly distinguishing the stellar sites hosting such a process. So, in realistic scenarios, the heavy elements produced may demonstrate a different abundance pattern which cannot be clearly stated as there are no evidences to conclude so. Hampel et al. (2016) also claim that the light-elements are not produced by a significant amount in the neutron-capture processes, but large production of ^{13}C and ^{14}N in PIEs are illustrated (Cristallo et al.

2009, 2016). So, multidimensional simulations are required for the *i*-process nucleosynthetic processes in order to accurately model the abundances of these light elements and their isotopic ratios (Herwig et al. 2011; Stancliffe et al. 2011; Herwig et al. 2014). Also, the effect of multiple PIEs to the enrichment of *ls* and *hs* are not available with current models. While the shorter neutron bursts can produce lighter *s*-peak elements, the longer neutron exposures produce the heavier *s*-peak elements (Koch et al. 2019). In the figure 14, the light *s*-process elements, Y and Zr are not well-fitted, so a combination of the individual neutron burst events may be required to model the lighter *s*-process elements. Moreover,

the number of neutron-capture elements detected in the spectra of our program stars are rather small. So it is not very clear that the heavy element enrichment in our program stars are produced only through a pure *i*-process or a mixture of other neutron-capture processes along with the *i*-process.

6 CONCLUSIONS

We studied 7 CEMP stars using both high-resolution optical spectra and low-resolution NIR spectra. We derived the O and $^{12}\text{C}/^{13}\text{C}$ ratio using optical and NIR spectra and found good agreement in the derived abundances. All the CEMP stars in this study exhibit enhancement in both carbon and neutron-capture elements and also show radial velocity variations. This favors AGB mass transfer scenario as a possible mechanism for the enhanced carbon and n-capture elements. Both the light element and the n-capture elements indicate accretion from a low-mass AGB companion. The abundance pattern of C, N and O is compared with AGB models of different masses and all the stars in this study are found to have low-mass low-metallicity AGB stars as companions. This low-mass nature of the companion is further confirmed by the Na abundances.

We demonstrated that low-resolution NIR observations can complement high resolution optical observations to derive the oxygen abundance and $^{12}\text{C}/^{13}\text{C}$ ratio in cool CEMP stars. Since the abundance of C, N can also be derived using low-resolution spectra, it may be proposed that low-resolution optical and NIR observations are adequate to constrain the nature of binary companion in cool CEMP stars. This will enable us to probe fainter cool CEMP stars thereby probe several cool CEMP stars beyond Milky Way. All the 7 CEMP stars studied here are identified to be exhibiting enhancements in both Ba and Eu. Among them, one of the stars (HE 1152-0355) exhibits $[\text{Ba}/\text{Fe}] > 1.0$, $[\text{Ba}/\text{Eu}] > 0.0$ and $[\text{Eu}/\text{Fe}] < 1.0$. These values sub-classify the star as a CEMP-*s* category. The low-mass AGB models fit well with the observed abundance pattern of HE 1152-0355. Rest of the 6 stars exhibit $[\text{Ba}/\text{Fe}] > 1.0$, $[\text{Ba}/\text{Eu}] > 0.0$ and $[\text{Eu}/\text{Fe}] > 1.0$. This indicates that these stars are enhanced in both *s*-process and *r*-process elements which sub-classify them as CEMP-*r/s*. Among the 6 stars, 5 stars are classified as CEMP-*r/s* in this study using their $[\text{Eu}/\text{Fe}]$ abundances which were not available earlier in literature thus they were wrongly classified as CEMP-*s* stars. The abundance pattern of the neutron-capture elements in these CEMP-*r/s* stars when compared with the models of *i*-process from Hampel et al. (2016) provides a good match. This support the idea of the operation of *i*-process in the inter-shell region of low-mass low-metallicity AGB stars for the production of heavy elements seen in the CEMP-*r/s* stars. While the Hampel et al. (2016) models provide a fairly good match in the fitting with the observed abundances, the light *s*-peak elements do not match well with the model as compared to the heavy *s*-peak elements. This may demand the inclusion of multiple PIEs of different neutron burst events which is currently not available with the existing models. Also, the number of neutron-capture elements detected in the spectra of program stars are somewhat smaller than required to differentiate between a pure *i*-process model and a mixture of neutron-capture events that would have contributed to the resultant abundance pattern. Even though the low-resolution optical and NIR spectroscopy is sufficient to constrain the mass and metallicity of the companion AGB star of cool CEMP stars, high-resolution studies can provide the better understanding of the nucleosynthetic origin of various elements present in them. Combining the key elements such as Li, C, N, O abundances and n-capture elements will pro-

vide valuable insights to various mixing mechanism and nuclear process that might have contributed to the observed abundances in CEMP-*r/s* stars.

ACKNOWLEDGEMENTS

We thank the anonymous referee for the useful comments. We thank the staff of IAO, Hanle and CREST, Hosakote, that made these observations possible. The facilities at IAO and CREST are operated by the Indian Institute of Astrophysics, Bangalore. AS and DKO acknowledge the support of the Department of Atomic Energy, Government of India, under Project Identification No. RTI4002. AS thanks Drisya Karinkuzhi for the fruitful discussions on different AGB models and *i*-process contributions to the enhancement of neutron-capture elements.

DATA AVAILABILITY

The data underlying this article will be shared on reasonable request to the corresponding author.

REFERENCES

- Abate C., Pols O. R., Izzard R. G., Karakas A. I., 2015, *A&A*, **581**, A22
 Alonso A., Arribas S., Martínez-Roger C., 1996, *A&A*, **313**, 873
 Alonso A., Arribas S., Martínez-Roger C., 1999, *A&AS*, **139**, 335
 Amarsi A. M., Asplund M., Collet R., Leenaarts J., 2016, *MNRAS*, **455**, 3735
 Amarsi A. M., Nissen P. E., Skúladóttir Á., 2019, *A&A*, **630**, A104
 Andrievsky S. M., Spite M., Korotin S. A., Spite F., François P., Bonifacio P., Cayrel R., Hill V., 2009, *A&A*, **494**, 1083
 Andrievsky S. M., Spite M., Korotin S. A., Spite F., Bonifacio P., Cayrel R., François P., Hill V., 2010, *A&A*, **509**, A88
 Aoki W., Tsuji T., 1997, *A&A*, **317**, 845
 Aoki W., Ryan S. G., Norris J. E., Beers T. C., Ando H., Tsangarides S., 2002, *ApJ*, **580**, 1149
 Aoki W., Beers T. C., Christlieb N., Norris J. E., Ryan S. G., Tsangarides S., 2007, *ApJ*, **655**, 492
 Aoki W., et al., 2013, *AJ*, **145**, 13
 Asplund M., Grevesse N., Sauval A. J., 2005, in Barnes III T. G., Bash F. N., eds, *Astronomical Society of the Pacific Conference Series Vol. 336, Cosmic Abundances as Records of Stellar Evolution and Nucleosynthesis*. p. 25
 Asplund M., Grevesse N., Sauval A. J., Scott P., 2009, *ARA&A*, **47**, 481
 Banerjee P., Qian Y.-Z., Heger A., 2018, *ApJ*, **865**, 120
 Barbuy B., Jorissen A., Rossi S. C. F., Arnould M., 1992, *A&A*, **262**, 216
 Baumüller D., Gehren T., 1997, *A&A*, **325**, 1088
 Beers T. C., Christlieb N., 2005, *ARA&A*, **43**, 531
 Beers T. C., Preston G. W., Shectman S. A., 1992, *AJ*, **103**, 1987
 Beers T. C., Sivarani T., Marsteller B., Lee Y., Rossi S., Plez B., 2007, *AJ*, **133**, 1193
 Bergemann M., Collet R., Amarsi A. M., Kovalev M., Ruchti G., Magic Z., 2017a, *ApJ*, **847**, 15
 Bergemann M., Collet R., Schönrich R., Andrae R., Kovalev M., Ruchti G., Hansen C. J., Magic Z., 2017b, *ApJ*, **847**, 16
 Bisterzo S., Gallino R., Straniero O., Cristallo S., Käppeler F., 2011, *MNRAS*, **418**, 284
 Bisterzo S., Gallino R., Straniero O., Cristallo S., Käppeler F., 2012, *MNRAS*, **422**, 849
 Bonifacio P., et al., 2015, *A&A*, **579**, A28
 Bonifacio P., et al., 2018, *A&A*, **612**, A65
 Busso M., Gallino R., Wasserburg G. J., 1999, *ARA&A*, **37**, 239

- Busso M., Wasserburg G. J., Nollett K. M., Calandra A., 2007, *ApJ*, **671**, 802
- Caffau E., Ludwig H. G., Steffen M., Livingston W., Bonifacio P., Malherbe J. M., Doerr H. P., Schmidt W., 2015, *A&A*, **579**, A88
- Campbell S. W., Lattanzio J. C., 2008, *A&A*, **490**, 769
- Campbell S. W., Lugaro M., Karakas A. I., 2010, *A&A*, **522**, L6
- Charbonnel C., 1995, *ApJ*, **453**, L41
- Charbonnel C., Brown J. A., Wallerstein G., 1998, *A&A*, **332**, 204
- Christlieb N., Green P. J., Wisotzki L., Reimers D., 2001, *A&A*, **375**, 366
- Clarkson O., Herwig F., Pignatari M., 2018, *MNRAS*, **474**, L37
- Cowan J. J., Rose W. K., 1977, *ApJ*, **212**, 149
- Cristallo S., Piersanti L., Straniero O., Gallino R., Domínguez I., Käppeler F., 2009, *Publ. Astron. Soc. Australia*, **26**, 139
- Cristallo S., et al., 2011, *ApJS*, **197**, 17
- Cristallo S., Karinkuzhi D., Goswami A., Piersanti L., Gobrecht D., 2016, *ApJ*, **833**, 181
- Cruz M. A., Serenelli A., Weiss A., 2013, *A&A*, **559**, A4
- Denissenkov P. A., Pinsonneault M., 2008, *ApJ*, **679**, 1541
- Denissenkov P. A., Herwig F., Battino U., Ritter C., Pignatari M., Jones S., Paxton B., 2017, *ApJ*, **834**, L10
- Denissenkov P. A., Herwig F., Woodward P., Androssy R., Pignatari M., Jones S., 2019, *MNRAS*, **488**, 4258
- Doherty C. L., Gil-Pons P., Siess L., Lattanzio J. C., Lau H. H. B., 2015, *MNRAS*, **446**, 2599
- Eggleton P. P., Dearborn D. S. P., Lattanzio J. C., 2008, *ApJ*, **677**, 581
- Fishlock C. K., Karakas A. I., Lugaro M., Yong D., 2014, *ApJ*, **797**, 44
- Gallagher A. J., Bergemann M., Collet R., Plez B., Leenaarts J., Carlsson M., Yakovleva S. A., Belyaev A. K., 2020, *A&A*, **634**, A55
- Goriely S., Demetriou P., Janka H. T., Pearson J. M., Samyn M., 2005, *Nuclear Phys. A*, **758**, 587
- Goswami A., Aoki W., Beers T. C., Christlieb N., Norris J. E., Ryan S. G., Tsangarides S., 2006, *MNRAS*, **372**, 343
- Gratton R. G., Sneden C., Carretta E., Bragaglia A., 2000, *A&A*, **354**, 169
- Hempel M., Stancliffe R. J., Lugaro M., Meyer B. S., 2016, *ApJ*, **831**, 171
- Hempel M., Karakas A. I., Stancliffe R. J., Meyer B. S., Lugaro M., 2019, *ApJ*, **887**, 11
- Hansen T., et al., 2015, *ApJ*, **807**, 173
- Hansen T. T., Andersen J., Nordström B., Beers T. C., Placco V. M., Yoon J., Buchhave L. A., 2016a, *A&A*, **586**, A160
- Hansen T. T., Andersen J., Nordström B., Beers T. C., Placco V. M., Yoon J., Buchhave L. A., 2016b, *A&A*, **588**, A3
- Hansen C. J., et al., 2016c, *A&A*, **588**, A37
- Hansen C. J., Hansen T. T., Koch A., Beers T. C., Nordström B., Placco V. M., Andersen J., 2019a, *A&A*, **623**, A128
- Hansen C. J., Hansen T. T., Koch A., Beers T. C., Nordström B., Placco V. M., Andersen J., 2019b, *A&A*, **623**, A128
- Hansen C. J., et al., 2020, *A&A*, **643**, A49
- Herwig F., 2004, *ApJS*, **155**, 651
- Herwig F., Pignatari M., Woodward P. R., Porter D. H., Rockefeller G., Fryer C. L., Bennett M., Hirschi R., 2011, *ApJ*, **727**, 89
- Herwig F., Woodward P. R., Lin P.-H., Knox M., Fryer C., 2014, *ApJ*, **792**, L3
- Jones S., Ritter C., Herwig F., Fryer C., Pignatari M., Bertolli M. G., Paxton B., 2016, *MNRAS*, **455**, 3848
- Jonsell K., Barklem P. S., Gustafsson B., Christlieb N., Hill V., Beers T. C., Holmberg J., 2006, *A&A*, **451**, 651
- Jorissen A., et al., 2016a, *A&A*, **586**, A158
- Jorissen A., et al., 2016b, *A&A*, **586**, A159
- Karakas A., Lattanzio J. C., 2007, *Publ. Astron. Soc. Australia*, **24**, 103
- Karinkuzhi D., Van Eck S., Goriely S., Siess L., Jorissen A., Merle T., Escorza A., Masseron T., 2021, *A&A*, **645**, A61
- Keller L. D., Pilachowski C. A., Sneden C., 2001, *AJ*, **122**, 2554
- Kennedy C. R., et al., 2011, *AJ*, **141**, 102
- Kipper T., Jorgensen U. G., 1994, *A&A*, **290**, 148
- Kobayashi C., Umeda H., Nomoto K., Tominaga N., Ohkubo T., 2006, *ApJ*, **653**, 1145
- Koch A., Reichert M., Hansen C. J., Hempel M., Stancliffe R. J., Karakas A., Arcones A., 2019, *A&A*, **622**, A159
- Kupka F., Piskunov N., Ryabchikova T. A., Stempels H. C., Weiss W. W., 1999, *A&AS*, **138**, 119
- Lattimer J. M., Schramm D. N., 1974, *ApJ*, **192**, L145
- Lind K., Primas F., Charbonnel C., Grundahl F., Asplund M., 2009, *A&A*, **503**, 545
- Lind K., Asplund M., Barklem P. S., Belyaev A. K., 2011, *A&A*, **528**, A103
- Lucatello S., Gratton R., Cohen J. G., Beers T. C., Christlieb N., Carretta E., Ramírez S., 2003, *AJ*, **125**, 875
- Lucatello S., Tsangarides S., Beers T. C., Carretta E., Gratton R. G., Ryan S. G., 2005, *ApJ*, **625**, 825
- Lucatello S., Beers T. C., Christlieb N., Barklem P. S., Rossi S., Marsteller B., Sivarani T., Lee Y. S., 2006, *ApJ*, **652**, L37
- Lucatello S., Masseron T., Johnson J. A., Pignatari M., Herwig F., 2011, *ApJ*, **729**, 40
- Lugaro M., Karakas A. I., Stancliffe R. J., Rijs C., 2012, *ApJ*, **747**, 2
- Lugaro M., et al., 2017, *Nature Astronomy*, **1**
- Mashonkina L., Christlieb N., 2014, *A&A*, **565**, A123
- Mashonkina L., Gehren T., 2000, *A&A*, **364**, 249
- Mashonkina L., Gehren T., Bikmaev I., 1999, *A&A*, **343**, 519
- Masseron T., Johnson J. A., Plez B., van Eck S., Primas F., Goriely S., Jorissen A., 2010, *A&A*, **509**, A93
- McClure R. D., Woodsworth A. W., 1990, *ApJ*, **352**, 709
- Mészáros S., et al., 2012, *AJ*, **144**, 120
- Meynet G., Ekström S., Maeder A., 2006, *A&A*, **447**, 623
- Ninan J. P., et al., 2014, *Journal of Astronomical Instrumentation*, **3**, 1450006
- Nollett K. M., Busso M., Wasserburg G. J., 2003, *ApJ*, **582**, 1036
- Nordlander T., Lind K., 2017, *A&A*, **607**, A75
- Palmerini S., Nollett K., Busso M., 2008, in *Nuclei in the Cosmos (NIC X)*.
- Pietrinferni A., Cassisi S., Salaris M., Castelli F., 2004, *ApJ*, **612**, 168
- Placco V. M., Frebel A., Beers T. C., Stancliffe R. J., 2014, *ApJ*, **797**, 21
- Plez B., 2012, *Turbospectrum: Code for spectral synthesis*, Astrophysics Source Code Library (ascl:1205.004)
- Plez B., Cohen J. G., 2005, *A&A*, **434**, 1117
- Prantzos N., Abia C., Limongi M., Chieffi A., Cristallo S., 2018, *MNRAS*, **476**, 3432
- Proffitt C. R., Michaud G., 1989, *ApJ*, **345**, 998
- Qian Y. Z., Wasserburg G. J., 2007, *Phys. Rep.*, **442**, 237
- Ramírez I., Meléndez J., 2005, *ApJ*, **626**, 465
- Reggiani H., et al., 2019, *A&A*, **627**, A177
- Salvadori S., Skúladóttir Á., Tolstoy E., 2015, *MNRAS*, **454**, 1320
- Sbordone L., et al., 2010, *A&A*, **522**, A26
- Sbordone L., Hansen C. J., Monaco L., Cristallo S., Bonifacio P., Caffau E., Villanova S., Amigo P., 2020, *A&A*, **641**, A135
- Schlegel D. J., Finkbeiner D. P., Davis M., 1998, *ApJ*, **500**, 525
- Schuler S. C., Hatzes A. P., King J. R., Kürster M., The L.-S., 2006, *AJ*, **131**, 1057
- Sivarani T., et al., 2004, *A&A*, **413**, 1073
- Sivarani T., et al., 2006, *A&A*, **459**, 125
- Smiljanic R., Gauderon R., North P., Barbuy B., Charbonnel C., Mowlavi N., 2009, *A&A*, **502**, 267
- Sneden C., et al., 2003, *ApJ*, **591**, 936
- Sneden C., Cowan J. J., Gallino R., 2008, *ARA&A*, **46**, 241
- Spite M., et al., 2005, *A&A*, **430**, 655
- Spite M., et al., 2006, *A&A*, **455**, 291
- Spite M., Caffau E., Bonifacio P., Spite F., Ludwig H. G., Plez B., Christlieb N., 2013, *A&A*, **552**, A107
- Sriram S., et al., 2018, in Evans C. J., Simard L., Takami H., eds, *Society of Photo-Optical Instrumentation Engineers (SPIE) Conference Series Vol. 10702, Ground-based and Airborne Instrumentation for Astronomy VII*. p. 107026K, doi:10.1117/12.2313165
- Stancliffe R. J., Glebbeek E., Izzard R. G., Pols O. R., 2007, *A&A*, **464**, L57
- Stancliffe R. J., Church R. P., Angelou G. C., Lattanzio J. C., 2009, *MNRAS*, **396**, 2313
- Stancliffe R. J., Dearborn D. S. P., Lattanzio J. C., Heap S. A., Campbell S. W., 2011, *ApJ*, **742**, 121
- Starkenburg E., Shetrone M. D., McConnachie A. W., Venn K. A., 2014, *MNRAS*, **441**, 1217

- Takeda Y., Zhao G., Chen Y.-Q., Qiu H.-M., Takada-Hidai M., 2002, [PASJ](#), **54**, 275
- Thielemann F. K., et al., 2011, [Progress in Particle and Nuclear Physics](#), **66**, 346
- Thielemann F. K., Eichler M., Panov I. V., Wehmeyer B., 2017, [Annual Review of Nuclear and Particle Science](#), **67**, 253
- Umeda H., Nomoto K., 2003, [Nature](#), **422**, 871
- Wasserburg G. J., Boothroyd A. I., Sackmann I.-J., 1995, [ApJ](#), **447**, L37
- Watson D., et al., 2019, [Nature](#), **574**, 497
- Wheeler J. C., Cowan J. J., Hillebrandt W., 1998, [ApJ](#), **493**, L101
- Winteler C., Käppeli R., Perego A., Arcones A., Vasset N., Nishimura N., Liebendörfer M., Thielemann F. K., 2012, [ApJ](#), **750**, L22
- Yanny B., et al., 2009, [AJ](#), **137**, 4377
- Yong D., et al., 2013, [ApJ](#), **762**, 26
- Yoon J., et al., 2016, [ApJ](#), **833**, 20
- Zhang H. W., Gehren T., Zhao G., 2008, [A&A](#), **481**, 489

APPENDIX A: ADDITIONAL TABLE OF SPECTRAL LINES USED FOR ABUNDANCE ANALYSIS

Element	λ	χ	$\log gf$
O I	6300.30	0.00	-9.72
Na I	5682.63	2.10	-0.71
Na I	5688.21	2.10	-0.45
Mg I	5528.41	4.35	-0.62
Mg I	5711.09	4.35	-1.83
Al I	6696.02	3.14	-1.35
Al I	6698.67	3.14	-1.65
K I	7664.91	0.00	0.13
K I	7698.97	0.00	-0.17
Ca I	5588.75	2.53	0.34
Ca I	6102.72	1.88	-0.79
Ca I	6122.22	1.89	-0.32
Ca I	6162.17	1.90	-0.09
Sc II	5526.79	1.77	0.02
Sc II	5658.36	1.50	-1.21
Sc II	5684.20	1.51	-1.07
Rb I	7800.26	0.00	0.14
Y II	5200.41	0.99	-0.57
Y II	5205.73	1.03	-0.34
Zr II	6127.48	0.15	-1.06
Zr II	6134.59	0.00	-1.28
Ba II	5853.68	0.60	-0.91
Ba II	6141.73	0.70	-0.03
La II	4920.97	0.13	-2.26
La II	5290.82	0.00	-1.65
La II	5301.97	0.40	-2.59
La II	5303.51	0.32	-1.87
La II	5797.57	0.24	-1.38
La II	5805.77	0.13	-1.59
Ce II	5187.46	1.21	0.30
Ce II	5274.23	1.04	0.13
Ce II	5330.56	0.87	-0.40
Pr II	5206.56	0.95	-0.16
Pr II	5207.90	0.80	-0.58
Pr II	5219.05	0.80	-0.05
Pr II	5259.73	0.63	0.11
Nd II	4811.34	0.06	-1.02
Nd II	5215.65	1.26	-0.65
Nd II	5249.58	0.98	0.09
Nd II	5276.87	0.86	-0.39
Nd II	5319.81	0.55	-0.14
Sm II	4777.84	0.04	-1.28
Sm II	4791.58	0.10	-1.24
Sm II	4815.80	0.19	-0.82
Sm II	4948.63	0.54	-0.85
Sm II	4952.37	0.33	-1.37
Sm II	5202.70	0.33	-1.65
Eu II	6645.09	1.38	0.12

APPENDIX B: ADDITIONAL FIGURES OF SPECTRAL FITTING

This paper has been typeset from a $\text{\TeX}/\text{\LaTeX}$ file prepared by the author.

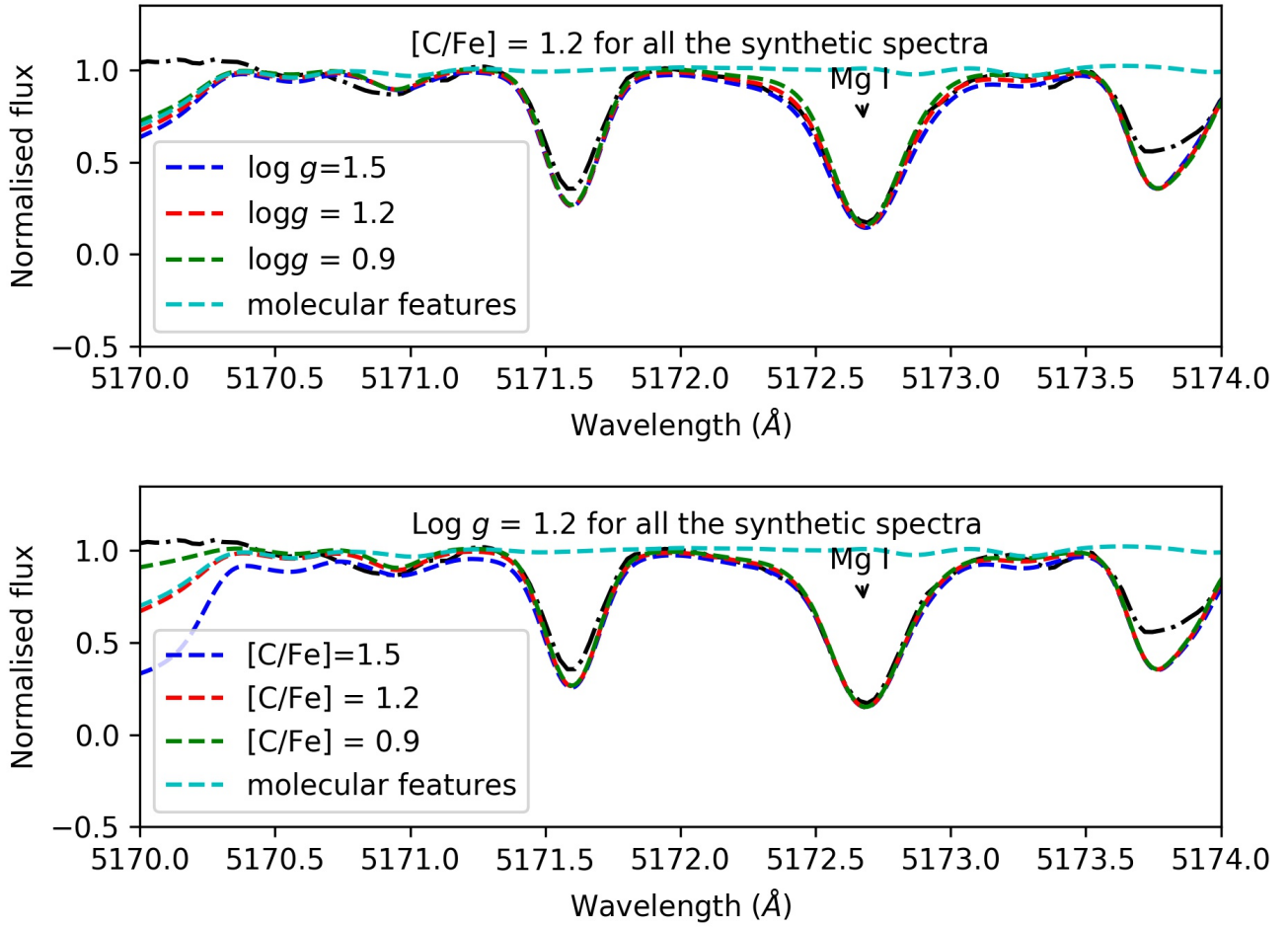


Figure B1. The effect of $\log g$ and Carbon abundance on Mg I lines are plotted. The top panel in the figure is the fitting of Mg I line at 5172 Å with different values of $\log g$ but with a fixed C abundance to show the sensitivity of $\log g$ to the Mg line wings. The bottom panel in the figure shows fitting of Mg I lines at 5172 Å with synthetic spectra of different values of C abundance but with a fixed value of $\log g$. It can be seen that, the C abundance does not have much effect on these Mg I lines.